



Structural, electrical, magnetic and magnetotransport properties of $\text{La}_{0.7}\text{Ca}_{0.18}\text{Ba}_{0.12}\text{Mn}_{0.95}\text{Sn}_{0.05}\text{O}_3$ manganite prepared with different quenching processes

Ibtihal Belal¹ · Faiza Meriche¹ · Nabil Mahamdioua² · Fatih Denbri² · Sevgi Polat-Altintas³ · Cabir Terzioglu³ · Jose Alonso Alonso⁴ · Jose Luis Martinez⁴

Received: 2 August 2022 / Accepted: 1 December 2022 / Published online: 13 December 2022
© The Author(s), under exclusive licence to Springer-Verlag GmbH, DE part of Springer Nature 2022

Abstract

Structural, microstructural, magnetic, electrical and magneto-transport properties of $\text{La}_{0.7}\text{Ca}_{0.18}\text{Ba}_{0.12}\text{Mn}_{0.95}\text{Sn}_{0.05}\text{O}_3$ manganite powders, prepared by the solid state method, were investigated. Two quenching processes were performed on the samples: quenching in air and quenching to 77 K in liquid nitrogen. X-ray diffraction patterns refinement revealed that the samples crystallized in the orthorhombic structure. The scanning electron microscopy micrographs presented granular characters. The magnetization vs temperature plot showed a paramagnetic-ferromagnetic transition. The inverse susceptibility $\chi^{-1}(T)$ deviation from the Curie–Weiss law revealed the existence of the phase above T_C in the nitrogen-quenched sample. The hysteresis cycles reveal that the samples are ferromagnetic at 1.8 K and paramagnetic at 300 K. The resistivity curves exhibit a ferromagnetic-metallic to paramagnetic-insulating transition. The magnetoresistance increased slightly in the sample quenched to 77 K in N_2 .

Keywords Perovskite manganites · Quenching · Structure · Magnetotransport properties · Magnetic properties · Double-exchange mechanism

1 Introduction

The perovskite manganites $\text{R}_{1-x}\text{A}_x\text{MnO}_3$ (R = rare earth ions such as Pr, La, Sm, Nd... and A = divalent earth ions such as Sr, Ba, Ca...) built up the interest of the researchers because of their potential use in solid oxide fuel cells (SOFC) [1], magnetic sensors [2], spintronics devices [3], magnetic refrigeration technology [4] and biomedical fields [5]. Manganite materials exhibit numerous properties, on can cite: charge ordering (CO), ferromagnetism (FM)

behavior, insulator–metal transition, colossal magnetoresistance (CMR) [6] and magnetocaloric effect [7, 8]. Such physical properties are principally explained through the superexchange interaction and double exchange (DE) mechanism. These two interactions are not sufficient to explain all the magnetoelectric behaviors in manganites other factors should be considered. According to the DE mechanism, the e_g electron mobility between two partially filled d shells causes the magnetic coupling between Mn^{3+} and Mn^{4+} (Hund's rule coupling), which leads to an FM interaction. However, the super exchange (SE) interaction produces an antiferromagnetic ordering [9]. As a result, depending on the $\text{Mn}^{3+}/\text{Mn}^{4+}$ ion ratio, these two magnetic behaviors can coexist in a single matrix. This type of competition is known as phase separation [10]. Meanwhile, the presence of FM clusters in the paramagnetic region is responsible for the existence of Griffiths phase in the temperature interval $T_C < T_G$ (T_G is the Griffiths temperature), which was originally suggested for a randomly diluted Ising ferromagnet [11].

Among the intriguing properties, the magneto-resistance (MR) and temperature coefficient of resistivity (TCR) are

✉ Faiza Meriche
fzmeriche@gmail.com

¹ LEM Laboratory, Department of Physics, Mohamed Seddik Ben Yahia University, 18000 Jijel, Algeria
² LEND Laboratory, Faculty of Sciences and Technology, Mohamed Seddik Ben Yahia University, 18000 Jijel, Algeria
³ Department of Physics, Faculty of Arts and Sciences, AIB University, 14280 Bolu, Turkey
⁴ Instituto de Ciencia de Materiales de Madrid, CSIC, Cantoblanco, 28049 Madrid, Spain

the most notable and extensively researched. In general, the MR and TCR maximum in manganites are observed near the metal–insulator transition (T_{MI}), which is followed by a FM to paramagnetic PM transition [12]. The TCR describes the sharpness of the M-I transition and characterizes the temperature sensitivity of the compounds. The temperature coefficient of resistivity with high values is suitable for infrared detectors [13]. The MR, on the other hand, describes the compounds' sensitivity to an applied external magnetic field. It is important to achieve the MR maximum at temperatures above 300 K for magnetic switching applications.

Various factors may affect the magnetic, electrical and magnetotransport properties. We can cite the most influential ones: Jahn–Teller effect [14], average A and/or B-site cation radius [15, 16], A-site cation size mismatch [17], oxidation degree of cations and oxygen deficiency [18, 19]. The effects of Mn-site replacement with a variety of elements such as Ni, Co, and Fe on the electrical and magnetic properties have been studied in many works [20, 21]. The authors deduced that the doping increased the electrical resistivity and magnetotransport properties of $\text{La}_{0.7}\text{Ca}_{0.3}\text{Mn}_{0.95}\text{X}_{0.05}\text{O}_3$ ($X = \text{Co}, \text{Fe}, \text{Cr}$ and Ni) manganite. Few studies have been conducted on the impact of Sn substitution at the Mn site on the manganite's properties. For instance, Li et al. reported that the addition of Sn leads to a significant drop in Curie temperature at low doping in $\text{La}_{0.5}\text{Ca}_{0.5}\text{Mn}_{1-x}\text{Sn}_x\text{O}_3$ ($0 \leq x \leq 0.06$) samples [22]. The influence of Sn substitution on the structural and magnetotransport properties of $(\text{La}_{0.67}\text{Sr}_{0.33})\text{MnO}_3$ has been investigated by Tank et al. [23]. The authors noticed the resistivity values increase and the T_{MI} transition temperature decreases. They reported that it could be due to the reduction in bandwidth caused by the large ionic radius of the Sn^{4+} substitution for Mn^{4+} . Kallel et al. examined the structural, magnetoresistance and magnetic properties of the $\text{La}_{0.7}\text{Sr}_{0.3}\text{Mn}_{1-x}\text{Sn}_x\text{O}_3$ system [24]. They revealed that the magnetoresistance increases for a low doping ratio ($x = 0.05$), which is discussed in light of the changes caused by Sn doping in the extrinsic MR and in the Mn^{3+} -O- Mn^{4+} network.

It is common knowledge that the conditions of the used elaboration method, such as sintering temperature, pressure, milling time and quenching process, have an effect on the physical properties of ceramics. To produce high-quality materials, these parameters must be carefully monitored and tuned. Many studies have reported on the effect of sintering temperature (T_s) on the structure, magnetic and electrical transport properties of $(\text{La}, \text{Ca})\text{MnO}_3$ manganite [25, 26]. They found that the magnetic entropy, magnetization, Curie and metal–insulator transition temperatures increased with sintering temperature, while the electrical resistivity decreased. V. Trukhanov et al. [27] studied the effect of pressure on the magnetic properties of $\text{La}_{0.7}\text{Sr}_{0.3}\text{MnO}_x$ manganites and found that the hydrostatic pressure increases the

FM part of the oxygen-deficient $\text{La}_{0.7}\text{Sr}_{0.3}\text{MnO}_{2.85}$. Effects of milling time and grinding speed on the structural and magnetic properties of the compound $\text{La}_{0.7}\text{Ca}_{0.3}\text{MnO}_3$ were investigated by W. Cherif et al. [28, 29]. They established that the Curie temperature, AC conductivity and grain size increased with the increase in milling time. However, only a few studies have been proposed to investigate the quenching process effect in manganite materials [30, 31]. The authors reported on the resistivity, magnetotransport and magnetization measurements on $\text{Pr}_{0.5}\text{Sr}_{0.5}\text{MnO}_3$ manganites quenched from 1400 °C to room temperature in water or in air. They found that magnetic and magneto-transport properties intensely depend on the quenching conditions.

In this paper, we studied the effect of the quenching process after the last sintering treatment on the physical properties of $\text{La}_{0.7}\text{Ca}_{0.18}\text{Ba}_{0.12}\text{Mn}_{0.95}\text{Sn}_{0.05}\text{O}_3$ (LCBMSO) manganite. For this purpose, we have carried out an analysis of the structural, microstructural, magnetic, electrical and magnetotransport properties of samples.

2 Experimental procedure

Polycrystalline samples of $\text{La}_{0.7}\text{Ca}_{0.18}\text{Ba}_{0.12}\text{Mn}_{0.95}\text{Sn}_{0.05}\text{O}_3$ (LCBMSO) were elaborated by the solid-state reaction method through the use of high-purity oxides La_2O_3 , SnO_2 , MnO_2 and carbonates BaCO_3 , CaCO_3 . The precursors were weighted and mixed in an agate mortar. To achieve decarbonization, the mixture was calcined at 900 °C for 14 h, then pressed into pellets of 13 mm diameter under 4 tons and sintered at 1150 °C/10 h, 1160 °C/10 h and 1170 °C/10 h with intermediate grinding and pressing. The two samples were cooled to room temperature in two different ways: one was quenched in air and the other was quenched to 77 K in liquid nitrogen. The obtained samples were structurally characterized at room temperature using a D8-Advance Bruker-AXS diffractometer with monochromatic Cu K_α radiation at $\lambda = 15406 \text{ \AA}$. The measurements were taken with a step of 0.016° for two seconds over an angular range of 2θ between 20° and 80.048° . The Rietveld refinement method was employed to analyze the recorded XRD patterns using the Fullprof program [32]. The compound morphology was observed by a scanning electron microscope (JEOL JSM-6390 LV type) equipped with an energy dispersive X-ray spectrometer (EDS). The magnetic measurements were performed at temperatures ranging from 1.6 to 300 K in zero-field cooled (ZFC) and cooled cooling (FCC) modes under 100 Oe using a SQUID magnetometer (MPMS-3, Quantum Design, USA). The electrical resistivity measurements $\rho(T, H)$ were carried out by using the standard four-probe method in the temperature range between 5 and 300 K, without and with the application of a 1 T magnetic field.

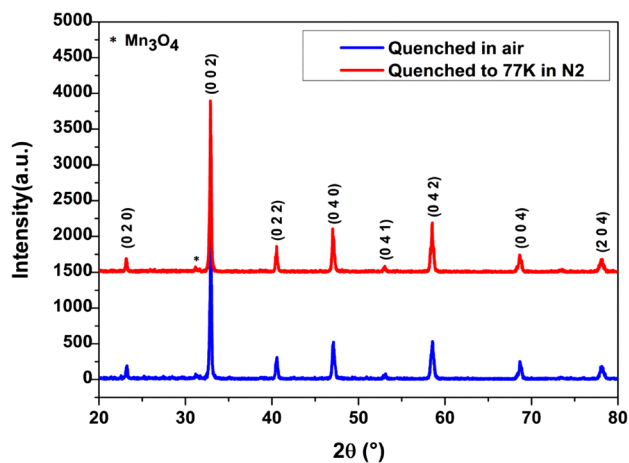


Fig. 1 XRD patterns of LCBMSO samples quenched in different ways

3 Results and discussion

3.1 X-ray diffraction analysis

XRD patterns of $\text{La}_{0.7}\text{Ca}_{0.18}\text{Ba}_{0.12}\text{Mn}_{0.95}\text{Sn}_{0.05}\text{O}_3$ samples quenched with different processes are shown in Fig. 1. The results reveal sharp and intense diffraction peaks, indicating the high crystallinity of our compounds. Figure 2 presents the Rietveld refinement results obtained using Fullprof software [32]. There is a good match between the experimental and simulated spectra. The refinement indicates that the samples are monophasic with an orthorhombic structure and Pnma space group. We note that the asterisk (*) in Fig. 1 denotes the presence a very low quantity of Mn_3O_4 impurity (JCPDS card, reference code. 00-001-1127) [33]. The inset in Fig. 2 displays the 3D representation of the compounds, showing the crystal structure and the MnO_6 octahedron. They are generated with the aid of VESTA software (Visualization for Electronic and Structural Analysis), using the Fullprof results in the output *.cif files [34]. The calculated unit cell parameters and volume (a , b , c , V) are summarized in Table 1, along with the refinement factors (R_p , R_{wp} , R_{Bragg} , R_F and $(\chi)^2$) and the crystallite size for the samples. The values of the refinement factors confirm the high quality of our refinement. One can see that the lattice parameters (a , b and c) verified the relationship of $a \approx b/\sqrt{2} \approx c$, implying that our samples own an orthorhombic structure [35]. A slight variation in unit cell parameters and volume is noticed.

The tolerance factor, noted t , is often calculated to see how stable the perovskite structure is by applying the following formula:

$$t = \frac{0.7(\text{La}^{3+}) + 0.18(\text{Ca}^{2+}) + 0.12(\text{Ba}^{2+}) + 3(\text{O}^{2-})}{\sqrt{2}(0.7\text{Mn}^{3+} + (0.3 - 0.05)\text{Mn}^{4+} + 0.05\text{Sn}^{4+})} \quad (1)$$

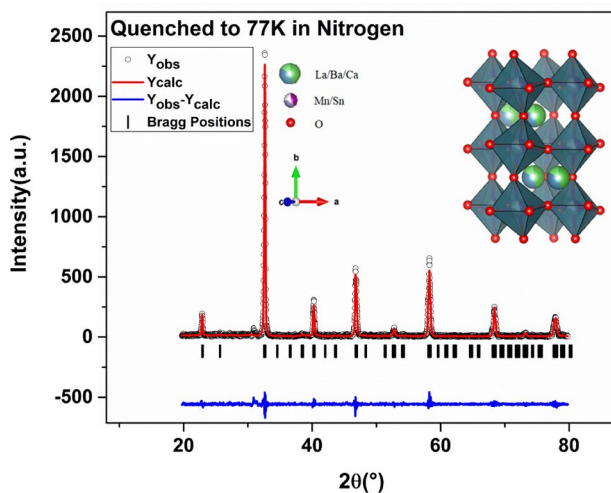
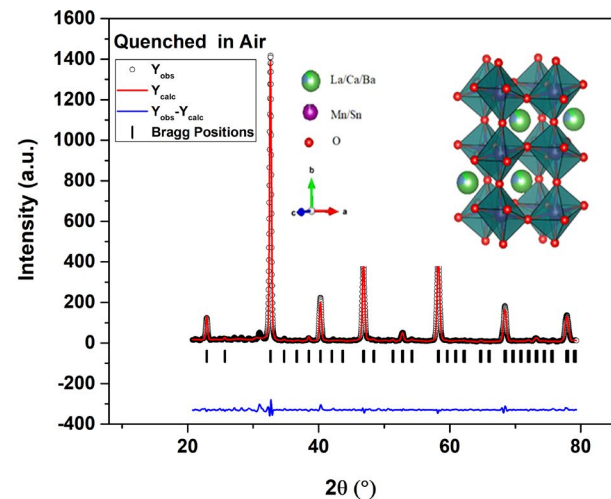


Fig. 2 Rietveld plots of XRD data for LCBMSO samples

where $\text{La}^{3+} = 1.216 \text{ \AA}$, $\text{Ca}^{2+} = 1.18 \text{ \AA}$ and $\text{Ba}^{2+} = 1.47 \text{ \AA}$ are the ninefold ionic radii of A-site; $\text{Mn}^{3+} = 0.645 \text{ \AA}$, $\text{Mn}^{4+} = 0.53 \text{ \AA}$, $\text{Sn}^{4+} = 0.69 \text{ \AA}$ and $\text{O}^{2-} = 1.35 \text{ \AA}$ are the sixfold ionic radii of B-site [36].

It is well known that the perovskite system is determined according to the tolerance factor value. When t is close to the unit, the structure is cubic. It is rhombohedral for $0.96 < t < 1$ and for $t < 0.96$ the system is orthorhombic [37]. In the present work, the calculated value of the tolerance factor t_{th} is 0.82, which indicates that the expected structure of our samples is orthorhombic. Moreover, the experimental tolerance factor reflects the degree of the octahedral distortion. It is given by Eq. (2) [38]:

$$t_{\text{exp}} = \frac{d_{A-O}}{\sqrt{2}d_{B-O}} \quad (2)$$

where d_{A-O} and d_{B-O} are the average bond lengths between A – O and B – O, respectively.

Table 1 Lattice parameters, unit cell volume with reliability factors, crystallite size and strain values calculated from Debye–Scherrer and Williamson Hall plot analysis

Sample	Quenched in air	Quenched to 77 K in N ₂
Lattice parameters		
<i>a</i> (Å)	5.4815(6)	5.5053(4)
<i>b</i> (Å)	7.7616(8)	7.7428(5)
<i>c</i> (Å)	5.4854(6)	5.4794(4)
<i>V</i> (Å) ³	233.38(17)	233.58(3)
Refinement factors		
<i>R_p</i> (%)	10.6	22.4
<i>R_{wp}</i> (%)	14.1	31.1
<i>R_{Bragg}</i> (%)	2.50	7.56
<i>R_F</i> (%)	3.15	14.7
χ ²	0.424	2.29
Average crystallite size		
<i>D_{SC}</i> (nm)	69.50	78.09
<i>D_{WH}</i> (nm)	74.15	88.31
ε (× 10 ⁻²)	0.146	0.154

For the ideal perovskite structure (tolerance factor $t = 1$), the Mn–O bond lengths in MnO₆ octahedra remain equal and the Mn–O–Mn bond angles equal 180°. When the perovskite structure is distorted (tolerance factor < 1), the MnO₆ octahedron tilting causes changes in the Mn–O bond lengths and the Mn–O–Mn bond angle becomes less than 180° [39]. From Table 2, we can see that the tolerance factor increases from 0.942 to 0.952 and the Mn/Sn–O–Mn/Sn bond angle gets closer to 180°, which leads to a reduction in the MnO₆ distortion. The increase in Mn/Sn–O–Mn/Sn angle promotes charge carrier hopping and decreases charge localization, which is backed up by resistivity data (discussed in the section below) [40]. It is noteworthy that the values of t_{th} and t_{exp} are in the orthorhombic interval $t < 0.96$; this indicates that the quenching process changes the bond lengths and the bond angles of the MnO₆ octahedron while the crystal structure remains orthorhombic.

In order to comprehend the quenching process effect on the crystallite size of our compound, Debye–Scherer’s formula [41] is used to estimate the crystallite size by taking the most intense XRD reflection peak (002) of both samples:

$$D_{sc} = \frac{K\lambda}{\beta \cos\theta} \quad (3)$$

where is $\lambda = 1.5406\text{Å}$ the X-ray wavelength, $K \cong 0.9$ is the shape factor, θ is the angle matching to the highest peak in the diffraction pattern and $\beta = \beta_{\text{sample}} - \beta_{\text{instrumental}}$

Table 2 Rietveld refined crystallographic parameters of LCBMSO samples, experimental tolerance factor, bandwidth
$$W = \frac{\cos\left(\frac{1}{2}(\pi - \langle \text{Mn-O-Mn} \rangle)\right)}{d_{(B-O)}^{2.5}}$$

and Jahn–Teller distortion given as

$$\delta_{JT} = \sqrt{\frac{1}{3} \sum_i^3 [(Mn-O)_i - \langle Mn-O \rangle]^2}$$

where Mn–O–Mn is the band angle d_{B-O} is the Mn–O bond length and $\langle Mn-O \rangle$ is the average bond length

Sample	Quenched in air	Quenched to 77 K in N ₂
Atomic position (La/Ca/Ba)		
<i>x</i>	0.01361	– 0.00546
<i>y</i>	0.25000	0.25000
<i>z</i>	– 0.00669	– 0.00313
<i>B_{iso}</i>	0.98305	0.77405
(Mn/Sn) <i>x</i>	0.00000	0.00000
<i>y</i>	0.00000	0.00000
<i>z</i>	0.50000	0.50000
<i>B_{iso}</i>	0.56834	0.50059
<i>O</i> (1) <i>x</i>	0.49666	0.49006
<i>y</i>	0.25000	0.25000
<i>z</i>	0.03638	0.05701
<i>B_{iso}</i>	0.02000	2.23215
<i>O</i> (2) <i>x</i>	0.25325	0.27128
<i>y</i>	–0.05055	0.02168
<i>z</i>	0.72151	0.74007
<i>B_{iso}</i>	0.02000	0.02528
Bond distance (Å)		
Mn–O1	1.95073	1.97304
Mn–O2	1.88611	1.90849
Mn–O2	2.07775	1.99729
<i>d_{A-O}</i>	2.6264	2.6404
<i>d_{B-O}</i>	1.9715	1.9596
Bond angles (°)		
$\langle \text{Mn/Sn-O-Mn/Sn} \rangle$	162.1009	162.7467
<i>t_{exp}</i>	0.9420	0.9520
<i>W</i> (eV)	0.0918	0.0938
δ _{JT}	0.0796	0.0375

is the line broadening at half of the maximum intensity (FWHM). The estimated crystallite size D_{SC} is found to be 69.5 nm in the sample quenched in air and has increased to 78.09 nm in the sample quenched to 77 K in liquid nitrogen. According to the Williamson–Hall method [42] more details can be obtained on the microstructures of our samples; the following relation was used:

$$\beta \cos\theta = \frac{K\lambda}{D_{WH}} + 4\epsilon \sin\theta \quad (4)$$

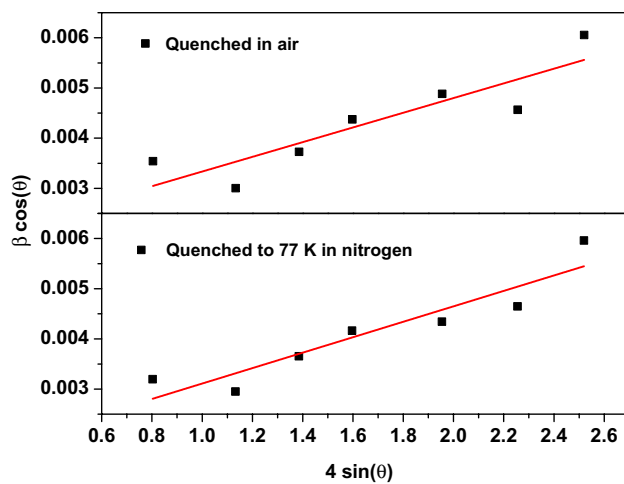


Fig. 3 Williamson-Hall plots for LCBMSO samples

The average crystallite size D_{WH} and lattice strain ϵ are calculated from the y-intercept and the slope of the linear plot of $\beta\cos\theta$ versus $4\sin\theta$ as shown in Fig. 3. The results display a positive slope that specifies the presence of positive or tensile stresses in the samples, which can lead to an increase in the cell volume as revealed by XRD analysis [43]. The estimated values of the strain and the crystallite size obtained from both the Debye–Scherrer and the Williamson-Hall methods are summarized in Table 1. From these results, we can conclude that the average crystallite size D_{WH} values are too higher than D_{SC} . The tensile stresses, which are considered in the Williamson-Hall analysis, can be responsible for this rise in values [44].

3.2 Morphological and elemental studies

Figure 4a, b represents SEM micrographs of the LCBMSO compounds quenched with two different processes. They are obtained from the surface of the pellets at the same magnification $3000\times$. The micrographs display granular surfaces nature for both samples. Grains with polygonal and spherical-like shapes of different sizes are formed. Needle-shaped grains appeared within the matrix of the quenched in air sample and a small number of them can be seen in the quenched in N_2 sample. Clearly visible grain boundaries and low porosity can be observed for the two samples. The average grain sizes are calculated using ImageJ software [45] without taking the needle-shaped grains into account and the sizes are found to be around 2.42 and 2.50 μm for samples quenched in air and quenched in N_2 , respectively.

Energy dispersive X-ray (EDX) spectra are presented in Fig. 5. All the elements detected from the EDX peak reflections belong to the constituent elements of the samples. The spectra show a peak related to carbon at low energy; it may be due to the incomplete decarbonization of the LCBMSO

compounds or to possible surface contamination caused by the use of sticking tape during the EDX characterization. Whereas the appearance of the Si peak can be attributed to the presence of silicate oxides [46]; we assume it only occurs on the surface since no trace of its phase was found in XRD diffractograms. The presence of silicate oxides in the matrix is most likely responsible for the production of needle-shaped grains.

3.3 Magnetization measurements data

The magnetization measurements were carried out in order to investigate the magnetic properties of $\text{La}_{0.7}\text{Ca}_{0.18}\text{Ba}_{0.12}\text{Mn}_{0.95}\text{Sn}_{0.05}\text{O}_3$ manganite samples. Magnetizations versus temperature (M-T) measurements have been recorded under a 100 Oe magnetic field for both samples. They were carried out in two modes. In zero-field cooled mode (ZFC), the samples were cooled down from room temperature to 1.6 K in the absence of a magnetic field and then magnetization data were collected up to 300 K by the application of a magnetic field of 100 Oe. In field-cooled cooling mode (FCC), magnetization data have been collected by cooling the samples again down to 1.6 K after applying a field of 100 Oe. The measured data are displayed in Fig. 6.

The ZFC and FCC magnetization curves are separated at irreversible temperatures $T_{irr}=120$ K for sample quenched in air and at $T_{irr}=122$ K for sample quenched to 77 K in liquid nitrogen. As the temperature dropped, the divergence between these curves widened significantly. However, this divergence is larger for the slow-cooled sample which is in our case the air-quenched one. The deviation between ZFC and FCC curves below T_{irr} may be due to the spin-glass nature of samples [47]. Figure 6 depicts that both samples exhibit an FM to PM transition at Curie temperature T_C . The magnetic transition shifted significantly toward high temperatures, as evidenced by the Curie temperature T_C determined from the minimum of dM/dT (Fig. 7). It is found to be at 140 K for the sample quenched in air and at 216 K for the sample quenched to 77 K in liquid nitrogen. The Curie temperature is proportional to the width of the e_g electron band ($T_C = \beta W$), where β is constant [48]. As a result, the increase in Mn/Sn – O – Mn/Sn angle from 162.1009° to 162.7467° and the decrease in Mn – O/Sn distance from 1.9715 Å to 1.9596 Å cause the increase in the bandwidth, which raises the T_C [49].

In the sections below, we have used the electronic bandwidth W to discuss the electrical properties of our samples. In addition, Fig. 7 shows another small dip in the differential magnetization curve of the sample quenched to 77 K in nitrogen, which corresponds to a temperature value higher than T_C . This can be attributed to the presence of ferromagnetic clusters within the paramagnetic region, as reported by Chihai et al. [50].

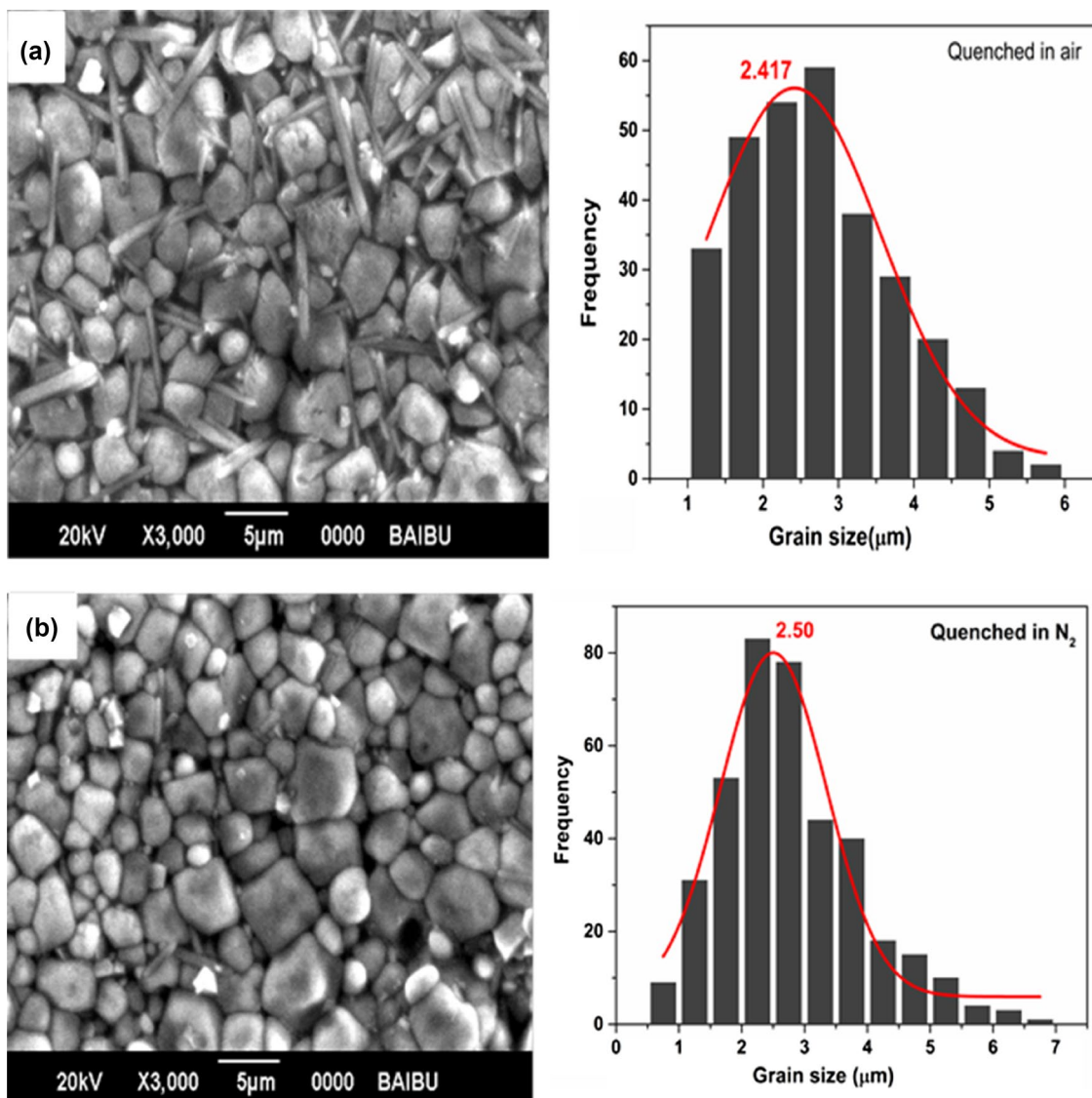


Fig. 4 SEM micrographs of the samples quenched with two different processes: **a** Quenched in air, **b** quenched in N₂ to 77 K and their respective particle average size distribution histograms

To get a better understanding of the magnetic behavior, we have plotted the inverse magnetic susceptibility [$\chi^{-1} = H/M$] versus temperature as depicted in Fig. 8. Contrary to the air-quenched sample, it shows that the nitrogen-quenched one presents a Griffiths phase between 258 and 318 K. It is well known that the relationship between C (the Curie constant) and T in the paramagnetic (PM) region should obey the Curie–Weiss (CW) law:

$$\chi = \frac{C}{T - \theta_p} \tag{4}$$

where θ_p is the Weiss temperature which can be estimated from the y-intercept of the Curie–Weiss plot $\chi^{-1}(T)$, the Curie constant C is extracted from the inverse of the slope.

The $\chi^{-1}(T)$ curve for the nitrogen-quenched sample presents a downturn deviation from CW law, which is absent for air-quenched one. This later adheres completely to the Curie–Weiss law.

The positive value of θ_p reveals the ferromagnetic interaction between the spins of our samples [51]. Moreover θ_p is greater than the T_C values for both samples. Commonly, the difference between T_C and θ_p depends on the substance and may be related to the existence of a short-range order, which could be caused by magnetic inhomogeneity [52].

Furthermore, we calculated the theoretical effective moment $\mu_{\text{eff}}^{\text{th}}$ and the experimental effective moments $\mu_{\text{eff}}^{\text{exp}}$ for both samples using the relations below [53–55]:

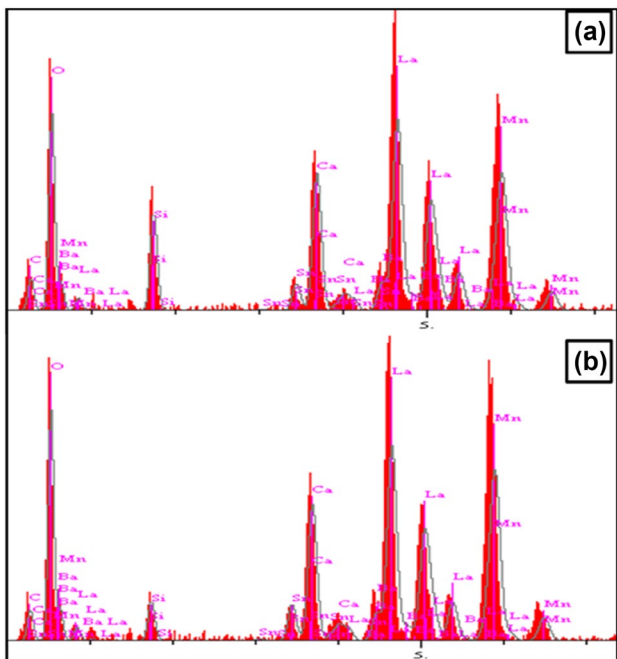


Fig. 5 EDX spectra of the samples **a** quenched in air and **b** quenched to 77 K in N₂

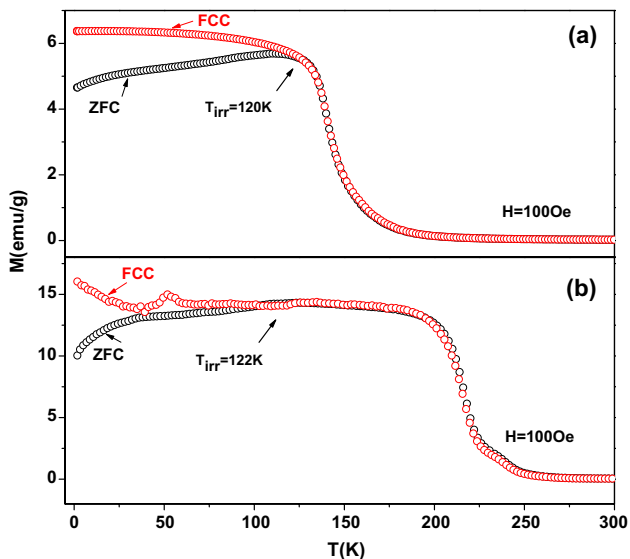


Fig. 6 Temperature-dependent ZFC and FC magnetization $M(T)$ in a field of $H=100$ Oe for samples: **a** quenched in air and **b** quenched to 77 K in nitrogen

$$\mu_{\text{eff}}^{\text{th}} = \sqrt{0.7 \times \mu_{\text{Mn}^{3+}}^2 + (0.3 - 0.05) \times \mu_{\text{Mn}^{4+}}^2} \quad (5)$$

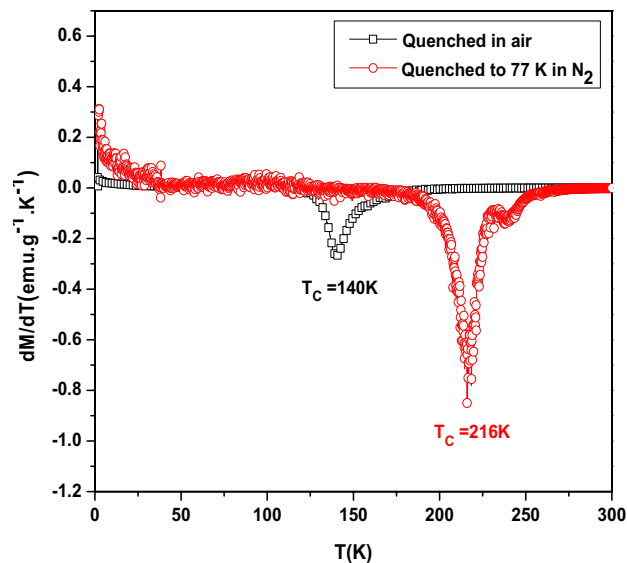


Fig. 7 Temperature dependence of differential magnetization curves at $H=100$ Oe

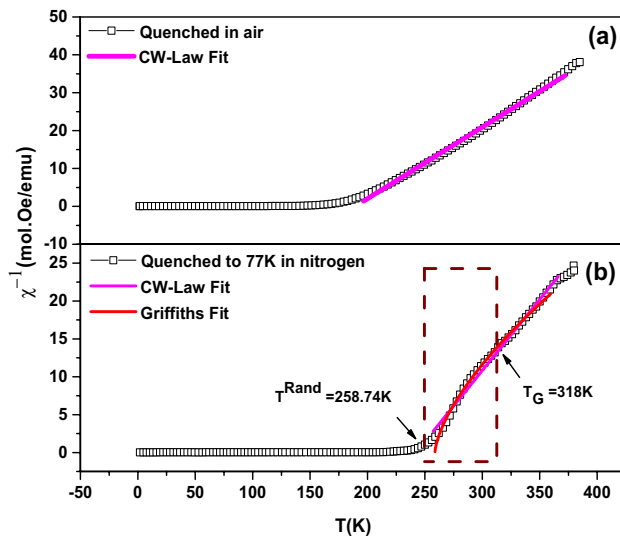


Fig. 8 Thermal dependence of inverse susceptibility ($\chi^{-1}=H/M$) of samples: **a** quenched in air and **b** quenched to 77 K in liquid nitrogen

$$\mu_{\text{eff}}^{\text{exp}} = \sqrt{\frac{3K_B C}{N_A \mu_B^2}} = \sqrt{8C} \mu_B \quad (6)$$

where $\mu_B = 9.27 \times 10^{-24} \text{ J.T}^{-1}$ is the Bohr magneton; $\mu_{\text{Mn}^{3+}} = 4.9\mu_B$; $\mu_{\text{Mn}^{4+}} = 3.87\mu_B$ [56]; $N_a = 6.023 \times 10^{23} \text{ mol}^{-1}$ the Avogadro number and $K_B = 1.38 \times 10^{-23} \text{ JK}^{-1}$ the Boltzmann constant. The obtained values of the C , T_C , θ_p , $\mu_{\text{eff}}^{\text{exp}}$ and $\mu_{\text{eff}}^{\text{th}}$ are

Table 3 Magnetic data for the two samples: quenched in air and quenched to 77 K in nitrogen

Sample	Quenched in air	Quenched to 77 K in N ₂
T_C (K)	140	216
T_G (K)	–	318
T^{Rand} (K)	–	258.74
θ_p (K)	189.3	242.2
C (emu.K/Oe.mol)	5.293	5.329
$\mu_{\text{eff}}^{\text{exp}}$ (μ_B)	6.507	6.529
$\mu_{\text{eff}}^{\text{th}}$ (μ_B)	4.533	4.533
λ	–	0.340

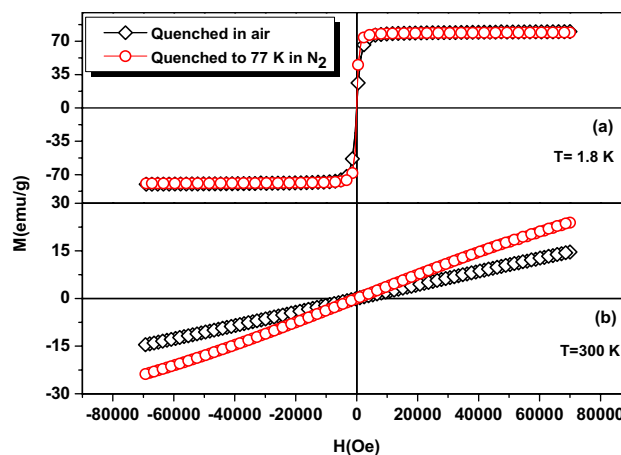
summarized in Table 3. As seen from the effective paramagnetic moment values, the experimental values are relatively much larger than the theoretical ones. The presence of ferromagnetic clusters in the paramagnetic region is at the origin of this difference [54]. These clusters could be caused by the Griffiths phase in the PM region [11].

It is worth noting that the susceptibility inverse deviates from CW law at Griffiths temperature T_G above T_C (see Fig. 8b). The boxed area in this figure represents the (GP) region, which is characterized by the existence of short range order of ferromagnetic clusters in a PM matrix. According to the Griffith's theory [11], this metaphase is distinguished by a susceptibility exponent (λ) which has a value between zero and unity. This exponent can be determined using the power law given by [57]:

$$\chi^{-1}(T) \propto (T - T^{\text{Rand}})^{1-\lambda} \quad (7)$$

where T^{Rand} represents the random FM temperature at which susceptibility tends to diverge ($T_C < T^{\text{Rand}} < T_G$). The fitted values of λ , T^{Rand} and T_G are mentioned in Table 3. The value of λ ($0 \leq \lambda \leq 1$) can be used to evaluate the strength of the Griffiths phase (GP). The exponent λ is expected to be zero in the pure PM region [58].

Figure 9 displays the variation of magnetization with an applied magnetic field between ± 70 kOe taken at temperatures of 1.8 K and 300 K for both samples. The M-H data was collected after cooling down the sample to 1.8 K. From this figure, one can notice that both samples exhibit a sharp rise in magnetization in the region of a weak magnetic field up to 10 kOe. Subsequently, the system reached saturation as the applied magnetic field increased. This proves the ferromagnetic character of our compounds as a result of the full orientation of the spins. At 300 K, magnetization changes linearly with magnetic field values, indicating that there is no saturation in magnetization, indicating that our samples

**Fig. 9** Magnetic hysteresis cycles at: **a** $T = 1.8$ K and **b** $T = 300$ K for both LCBMSO samples

are paramagnetic at this temperature. We can observe a difference between the curve levels of the two samples, which may be attributed to the difference in the grain sizes. In fact, the nitrogen-quenched sample, with higher mean grain sizes, exhibits a higher level curve. This result is in accordance with those found by P. Kameli et al. [59] and by V. Dyakonov et al. [60].

3.4 Electrical and magneto-electrical properties

The electrical resistivity $\rho(T)$ without and with a 1 T applied magnetic field and the magnetoresistance (MR) as a function of temperature for our compounds quenched in different ways are shown in Fig. 10. Both samples possess a metal-insulator transition at T_{MI} , which is the temperature at the obtained resistivity maximum. Semiconductor behavior is above T_{MI} and metallic behavior is below it. In addition, Fig. 10 displays the magnetoresistive character as manifested by the significant decrease in resistivity with the application of a magnetic field. One can notice that T_{MI} values move towards high temperatures, implying that the applied magnetic field promotes electron hopping between adjacent Mn ions, and this finding is in agreement with the double-exchange (DE) model [61, 62]. We note that the resistivity values change according to the quenching process. The largest value is obtained for the sample quenched in air (see Fig. 11). It should be emphasized that the resistivity values in the granular manganites are considerably related to the grain size. It is found to be lower in samples with larger grains and this has been explained by the fact that grain boundaries include more magnetic disorder, which increases electron scattering [63].

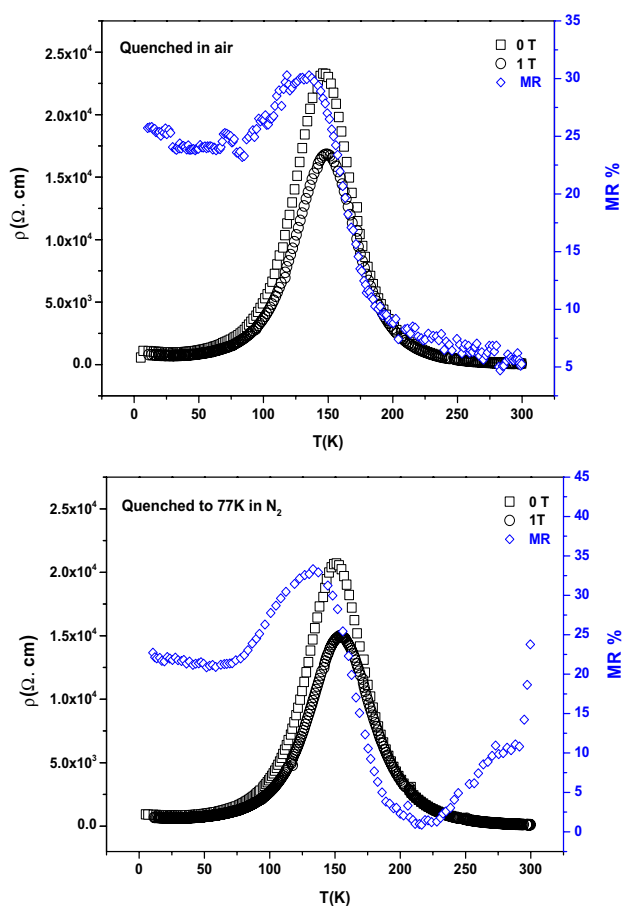


Fig. 10 Temperature variation of resistivity at 0 and 1 T and magnetoresistance MR% of LCBMSO compounds

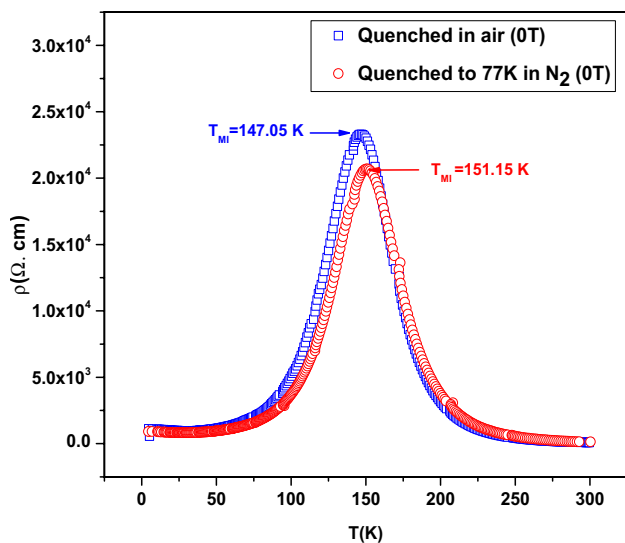


Fig. 11 Temperature variation of the resistivity of LCBMSO compounds

From the refined results of the Rietveld method of Mn/Sn – O – Mn/Sn angles and Mn/Sn – O distances (Table 2), one can explain the electron hopping behavior between the Mn/Sn – O sites based on electronic bandwidth values [61]. In this regard, the Mn/Sn – O – Mn/Sn angle is proportional to the electronic bandwidth W [64], which is empirically described by the following expression:

$$W = \frac{\cos\left(\frac{1}{2}\pi - \langle \text{Mn} - \text{O} - \text{Mn} \rangle\right)}{d_{(B-O)}^{3.5}} \tag{8}$$

where $\langle \text{Mn} - \text{O} - \text{Mn} \rangle$ is the bond angle and $d_{(B-O)}$ is the Mn – O bond distance. From Table 2, we notice that there are three different Mn/Sn – O distances, which indicates that the structure is distorted. Such distortion is mainly due to the ionic radius of the constituent elements and the Jahn–Teller effect. According to Eq. (8), the enlargement in the bond angle Mn – O – Mn and the decrease in bond distance Mn – O cause the increase in the electronic bandwidth W [65]. According to our findings, the W is smaller in the case of the sample quenched in air than in the sample quenched to 77 K in liquid nitrogen. The increase in bandwidth values increases the overlapping of the Mn-3d and O-2p orbitals resulting in an increase in the exchange coupling of $\text{Mn}^{3+} - \text{O}^{2-} - \text{Mn}^{4+}$. In an insulator, the gap energy E_g is described as $E_g = \Delta - W$; Δ represents the charge transfer energy. Indeed, in $\text{R}_{1-x}\text{A}_x\text{MnO}_3$ manganite, the Δ changes sparsely and the bandwidth W becomes the major factor controlling the E_g band [66]. As a result, increasing W decreases the E_g band, resulting in a high metal–insulator temperature T_{MI} and a low peak of resistivity in the sample quenched to 77 K (see Fig. 11).

Furthermore, the change in the quenching process affects the experimental tolerance factor and the JTD distortion. This later is calculated according to the following relation [64]:

$$\delta_{JT} = \sqrt{\frac{1}{3} \sum_i^3 [(\text{Mn} - \text{O})_i - \langle \text{Mn} - \text{O} \rangle]^2} \tag{9}$$

The degeneration of the Mn 3d orbital in manganites is lifted by its splitting into t_{2g} and e_g orbitals as a result of the influence of the octahedral crystal field. However, in the presence of Jahn–Teller distortion, further splitting of the e_g and t_{2g} orbitals occurs, which leads to the localization of the electrons [67]. From Table 2, we notice the decrease in the MnO_6 octahedral distortion values with the increase in grain size. This diminution is in accordance with the increase in the e_g electron delocalization; consequently, the resistivity decreases.

Table 4 Resistivity values, metal–insulator transition temperature T_{MI} , maximum of magnetoresistance MR_{max} and maximum of temperature coefficient of resistivity TCR_{max}

Sample	H (T)	ρ (Ω cm)	T_{MI} (K)	TCR_{max} %	MR_{max} %
Quenched in air	0	23,298.50	147.05	4.47 / T = 109 K	30.08
	1	16,830.69	149.22	4.32 / T = 107 K	
Quenched to 77 K in nitrogen	0	20,696.36	151.15	4.42 / T = 119 K	33.31
	1	14,882.39	155.79	4.13 / T = 120 K	

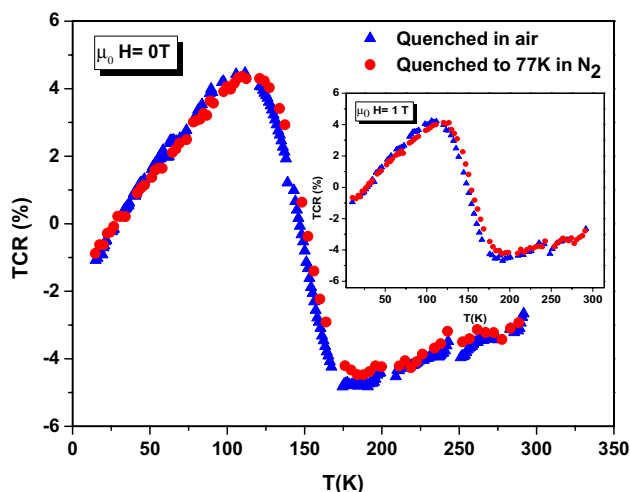


Fig. 12 Variation in $TCR\%$ with temperature at 0 and 1 T for LCBMSO compounds

The temperature-dependent magnetoresistance is given by the following expression:

$$MR\% = \frac{\rho(0) - \rho(H)}{\rho(0)} \times 100 \tag{10}$$

where $\rho(0)$ and $\rho(H)$ are the resistivities at zero and 1 T of applied magnetic fields, respectively. The effect of MR is observed over a wide temperature range from 5 to 300 K. The MR exhibited a maximum ratio of 33% around T_{MI} in the MR-T curves for the sample quenched to 77 K in liquid nitrogen (Fig. 10). One can see that the magnetoresistance is more pronounced in the metallic region, as expected. Resistivity values, metal-insulation transition and the magnetoresistance MR_{max} are tabulated in Table 4.

The temperature coefficient of resistivity in the nearness of T_{MI} is very useful in bolometric and infrared detectors [68, 69]. Figure 12 displays the effect of the quenching process and magnetic field application on the TCR. This parameter is described by the following equation:

$$TCR(\%) = \left(\frac{1}{\rho} \times \frac{d\rho}{dT} \right) \times 100 \tag{11}$$

where ρ and T are the resistivity and the temperature. The maximum of TCR value is 4.47% at 109 K for the sample quenched in air and 4.42% at 119 K for the sample quenched to 77 K in nitrogen. There is no change in its curves when a 1 T external magnetic field is applied. Our TCR_{max} values are significantly lower than those found in previous works [68–71], however, they are high in comparison with values reported by other studies [69, 72]. We assume that the differences are primarily due to the elaboration conditions.

3.5 Conduction mechanism

With the aim of better understanding the conduction mechanism of our materials, we employed many models to fit our $\rho(T)$ curves. These models include a number of interactions that could alter the magneto-transport properties of our samples [73].

3.5.1 Low-temperature behavior ($T < T_{MI}$)

In the ferromagnetic phase, the electrical conduction below the M-I transition is mainly understood according to the double-exchange theory [74]. However, some details on the variation of low temperature resistivity ($T < T_{MI}$) and interactions between the different scattering mechanisms resulting from various contributions are not completely understood [75]. We have fitted our temperature-dependent resistivity data using different models. These models are described as a combination of a number of interactions and given by the following relations:

$$\rho = \rho_0 + \rho_5 T^5 \tag{12}$$

$$\rho = \rho_0 + \rho_2 T^2 + \rho_5 T^5 \tag{13}$$

$$\rho = \rho_0 - \rho_{0.5} T^{0.5} + \rho_2 T^2 + \rho_5 T^5 \tag{14}$$

where ρ_0 is the resistivity induced by the grain boundary effect, the term $\rho_{0.5} T^{0.5}$ represents the weak localization [76]; the electrical resistivity $\rho_2 T^2$ in Eqs. (13) and (14) described the electron–electron scattering contribution [77]; the electron–phonon scattering processes is introduced in the last term $\rho_5 T^5$ [78].

The accuracy of our fits is assessed by comparing the obtained values of the squared linear correlation coefficients R^2 . The best results for both samples with and without

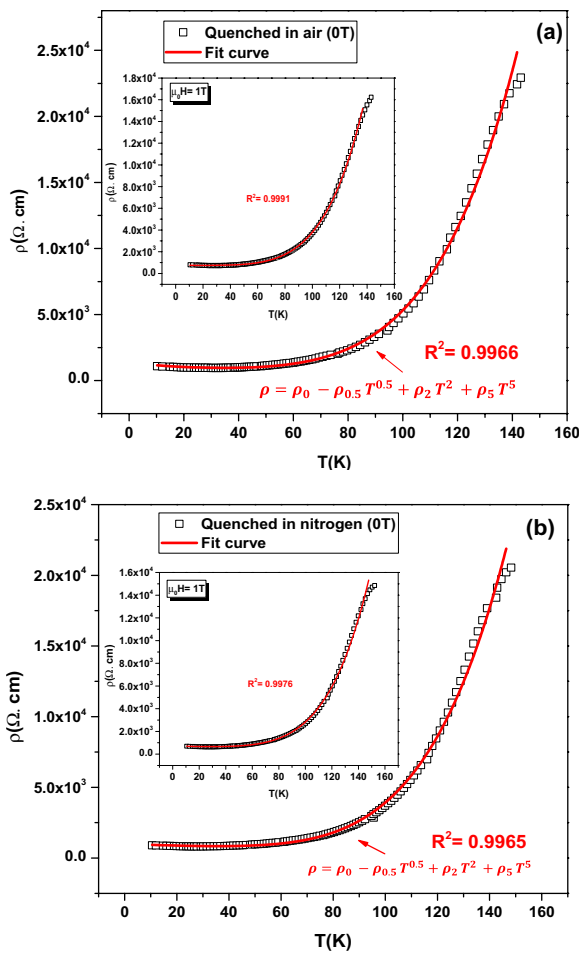


Fig. 13 Fit curves of resistivity versus temperature for LCBMSO samples by weak localization (ee-ep): **a** quenched in air and **b** quenched to 77 K in nitrogen

applied magnetic fields are related to the model with the four terms in Eq. (14). They are displayed in Fig. 13. The R^2 value is found to be around 0.996. In Table 5, the best fit parameters are listed. As can be seen, applying a magnetic field decreases the ρ_0 , $\rho_{0.5}$, ρ_2 and ρ_5 values. This could be understood by the overall reduction of the spin fluctuation with the application of an external magnetic field [63].

Moreover, the ρ_0 , $\rho_{0.5}$, ρ_2 and ρ_5 values are found to considerably decrease in the case of the sample quenched in

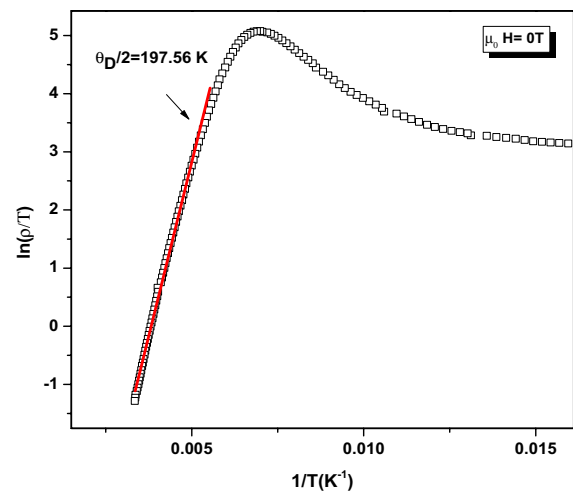


Fig. 14 Determination of Debye temperature for LCBMSO sample quenched in air under zero tesla magnetic field

nitrogen. This is expected since the resistivity values also decrease. Such a decrease reflects the eventual lowering in scattering processes due to grain enlargement compared to the air quenched sample [79]. We notice from the obtained values that the term ρ_0 , which represents the residual resistivity, is larger than the terms $\rho_{0.5}T^{0.5}$, ρ_2T^2 and ρ_5T^5 , this indicates that in the conduction process, grain boundaries play a crucial role.

3.5.2 High-temperature behavior ($T > T_{MI}$)

Various models can be used to explain the variation in the electrical resistivity with temperature above T_{MI} , for instance: Adiabatic small polaronic conduction (ASPC) [80], Thermally activated conduction (TAC) [80], Mott's variable range hopping (VRH) [35], Biadiabatic small polaron hopping (BASPH) [81], Non-adiabatic small polaron hopping (NASPH) [75], Holstein's adiabatic small polaron (HASPH) [82] and the Effros-Schklovskii variable range hopping (ES-VRH) model [83]. From the fitting study performed on our samples, we have adopted small polaron hopping and 3D Mott's variable range hopping models [84], in two complementary regions separated by the Debye temperature (θ_D). This temperature is estimated from the plot of $\ln(\rho/T)$ vs

Table 5 Low temperature best fit parameters obtained for our samples

Sample	H (T)	ρ_0 (Ω cm)	$\rho_{0.5}$ (Ω cm $K^{-0.5}$)	ρ_2 (Ω cm K^{-2})	ρ_5 ($\times 10^{-7}$) (Ω cm K^{-5})	R^2
Quenched in air	0	1536.1079	121.7179	0.1047	3.9612	0.9966
	1	770.7879	6.1259	0.0108	2.9769	0.9991
Quenched to 77 K in nitrogen	0	1088.939	48.8392	0.0207	3.1183	0.9965
	1	772.5499	25.2730	0.0284	2.0229	0.9976

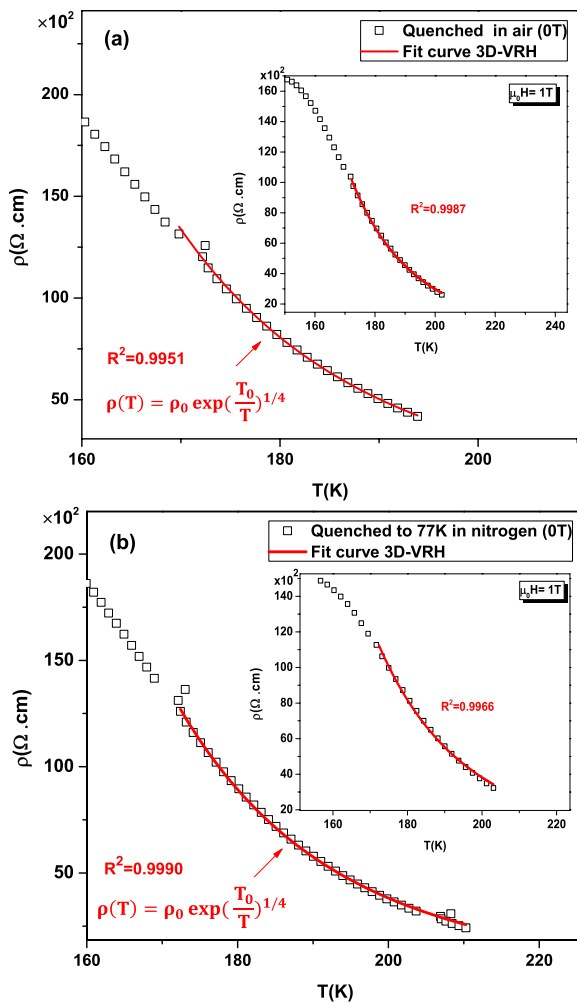


Fig. 15 Fit curve of resistivity versus temperature by 3D-VRH for samples: **a** quenched in air and **b** quenched to 77 K

($1/T$) shown in Fig. 14. The 3D Mott’s variable range hopping model is given as follows:

$$\rho(T) = \rho_0 \exp\left(\frac{T_0}{T}\right)^{1/4} \tag{15}$$

where $\rho(T)$ is the experimental resistivity, T_0 is the characteristic temperature, ρ_0 is the residual resistivity. The obtained values of T_0 are similar to those mentioned for other manganites [85].

In addition, the density of state near the Fermi level $N(E_F)$ can be calculated using the following equation [86]:

$$K_B T_0 = 24 / (\pi N(E_F) \xi^3) \tag{16}$$

where, $N(E_F)$ is the density of states near the Fermi level, K_B is the Boltzmann constant and ξ is the localization length, usually taken to be 0.45 nm [87].

The obtained Mott parameter T_0 allowed us to determine the density of state $N(E_F)$ for both samples. The fitting curves are shown in Fig. 15.

The estimated parameters $N(E_F)$ and T_0 are provided in Table 6, and they are consistent with previous works [88, 89]. We note here that the $N(E_F)$ of the sample quenched in nitrogen is the largest one. This value gives electrons more opportunities to hop; which improve conductivity values.

Moreover, the applied magnetic field leads to an increase in $N(E_F)$ for both samples, which explains the decrease in resistivity and hence the magnetoresistive character of the samples. In order to understand which of the two samples is more magnetoresistive than the other, we calculate the $\Delta N(E_F)$ given by:

$$\Delta N(E_F) = N(E_F)_{1T} - N(E_F)_{0T} \tag{17}$$

$N(E_F)_{1T}$ and $N(E_F)_{0T}$ are the densities of state at 1 and 0 T.

From Table 6, we can see that $\Delta N(E_F)$ for the 77 K quenched sample is larger than the air quenched one. This means that the quenched sample at 77 K is more sensitive to the magnetic field and thus more magnetoresistive.

According to the 3D-VRH, the expressions of the mean hopping distance R_h and mean hopping energy E_h can be written [90] as follows:

$$R_h(T) = \frac{3}{8} \xi \left(\frac{T_0}{T}\right)^{1/4} \tag{18}$$

$$E_h = \frac{1}{4} k_B T^{3/4} (T_0)^{1/4} \tag{19}$$

The findings are presented in Figs. 16 and 17.

One can see that R_h values decrease with increasing temperature, contrary to E_h values; this is the main character of the VRH mechanism, which translates the “intelligent” hopping of the electrons. The obtained values of the mean hopping distance R_h are greater than the Mn – O – Mn distance of 0.39 nm [91, 92].

It is worth noting that the mean hopping energy E_h for the sample quenched in 77 K is greater than the E_h values for the other sample. Under a zero field, the obtained value of E_h for the sample quenched in air varies between 0.117 eV and 0.145 eV; it ranges between 0.111 eV and 0.138 eV for the sample quenched to 77 K in nitrogen.

It is commonly known that the electrical resistivity above $\theta_D/2$ can be investigated using the adiabatic small polaron hopping (ASPH) model [26, 93, 94], which is identified by the following expression:

$$\rho(T) = \rho_0 T \exp\left(\frac{E_a}{K_B T}\right) \tag{20}$$

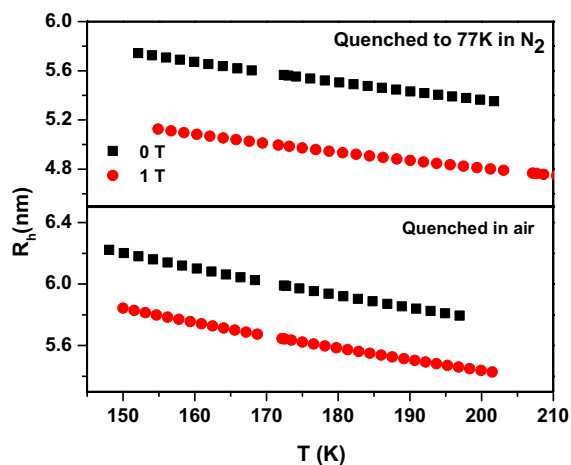


Fig. 16 Mean hopping distance of LCBMSO compounds

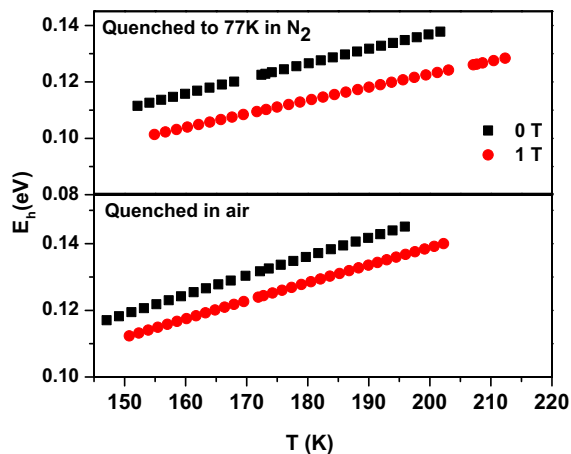


Fig. 17 Mean hopping energy of LCBMSO compounds

where ρ_0 is the residual resistivity and E_a denotes the activation energy for electrical conductivity. Figure 18 displays the ASPH model's results. The estimated values of activation energy for this model are recapitulated in Table 7.

In sum, based on the findings obtained in this section, we conclude that the semiconductor phase is well described by the suitable model in each region.

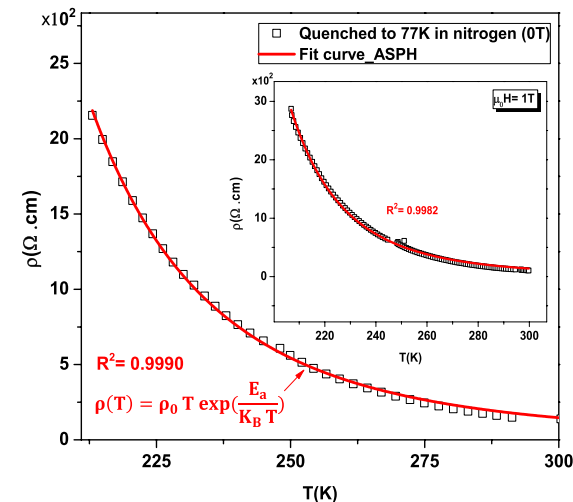
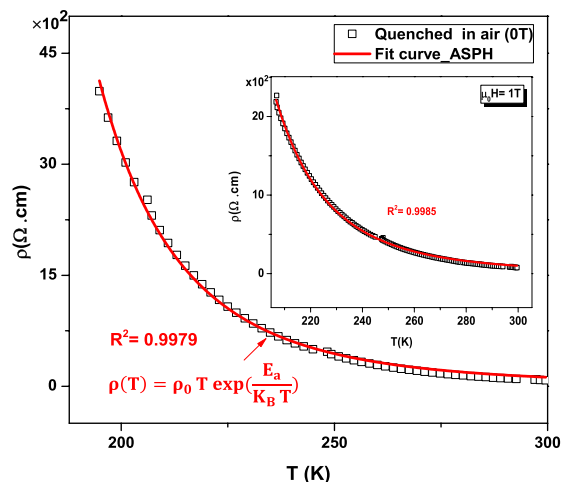


Fig. 18 Fit curves of resistivity versus temperature for the samples by ASPH model: a quenched in air and b quenched to 77 K in nitrogen

4 Conclusion

In conclusion, an investigation of the quenching effects on the structural, magnetic, electrical and magneto transport properties of $La_{0.7}Ca_{0.18}Ba_{0.12}Mn_{0.95}Sn_{0.05}O_3$ compounds elaborated by the solid-state route has been reported. XRD patterns and Rietveld refinements revealed that the structure of the two samples was orthorhombic with Pnma space group. The calculated crystallite size increased from 69.5 nm for the sample quenched in air to 78.09 nm for the sample quenched to 77 K in liquid nitrogen. The samples

Table 6 Fitting parameters using 3D-VRH model

Sample	H (T)	ρ_0 (Ω cm)	T_0 (K)	$N(E_F)$ ($eV^{-1} cm^{-3}$)	$\Delta N(E_F)$	R^2
Quenched in air	0	4.515×10^{-12}	2.738×10^8	3.555×10^{18}	0.957	0.9951
	1	2.998×10^{-11}	2.157×10^8	4.512×10^{18}		0.9987
Quenched to 77 K in nitrogen	0	6.005×10^{-11}	2.041×10^8	4.769×10^{18}	2.61	0.9990
	1	1.603×10^{-9}	1.319×10^8	7.379×10^{18}		0.9966

Table 7 Fitting parameters using ASPH model

Sample	H (T)	$\theta_D/2$ (K)	ρ_0 (Ω cm)	T_0 (K)	E_a (eV)	R^2
Quenched in air	0	197.56	2.661×10^{-4}	2199.384	0.1897	0.9979
	1	203.79	1.478×10^{-4}	2313.361	0.1996	0.99859
Quenched to 77 K in nitrogen	0	203.79	2.835×10^{-4}	2236.470	0.1929	0.9990
	1	213.67	2.407×10^{-4}	2266.234	0.1955	0.99825

possess a granular morphology. The magnetic properties of our samples were assessed in both zero field and field cooling magnetization modes. Both samples showed a FM-PM transition and T_c became higher with the enlargement of Mn/Sn – O – Mn/Sn bond angle. The Curie–Weiss law and the Griffiths phase function are used to fit all curves. The existence of a short-range order of ferromagnetic clusters in a paramagnetic region revealed the presence of the Griffiths phase, in the nitrogen quenched sample. The $\rho(T)$ curves showed a metal–insulator transition at 151.15 and 147.05 K for the quenched samples to 77 K and in air, respectively. The resistivity reduction induced by the application of a magnetic field is explained by the double exchange theory. The maximum value of magnetoresistance is 33% for the sample quenched in liquid nitrogen. The maximum value of the temperature coefficient of resistivity is 4.47% for the sample quenched in air. In the metal region $T < T_{MI}$, the resistivity data are found to fit well by using a combination of interactions: weak localization, residual resistivity, electron–phonon interaction and electron–electron scatterings. In the insulating region $T > T_{MI}$, the electrical resistivity data fit well with two models: Mott's variable range hopping (3D-VRH) and the adiabatic small polaron hopping model (ASPH). The calculated parameters such as Mn/Sn – O distance, Mn/Sn – O – Mn/Sn angle, Jahn–Teller distortion, bandwidth and density of state $N(E_F)$ are found to be coherent with each other and are used in this study to explain why the sample quenched in nitrogen to 77 K is the most magnetoresistive.

Acknowledgements This work was supported by the General Direction of Scientific Research and of Technological Development of Algeria (DGRSDT/MESRS).

Author contributions NM conceived of the presented idea. IB, FM, and NM prepared the samples. NM, FM conceived and planned the experiments. IB, FD, SPA and CT, carried out the structural, microstructural and magneto-electrical measurements. JAA and JLM carried out the magnetic measurements. IB simulated and discussed the refinement of the XRD patterns. IB, FM and NM carried out and discussed the simulation results of the magnetic and the magneto-electrical experimental data. IB, FM and NM wrote the manuscript. All authors discussed the results, contributed, and commented on the final manuscript. FM and NM supervised the project.

Data availability The datasets generated during and/or analysed during the current study are available from the corresponding author on reasonable request.

Declarations

Conflict of interest The authors declare that there is no known conflict of interests regarding the publication of this paper.

References

1. E.S.M. Seo, A.A. Couto, N.B. Lima, A.C. Kohler, E.P. Soares, Properties of Sr-doped lanthanum manganites for SOFC. *Mater. Sci. Forum* **416**, 354–358 (2003). <https://doi.org/10.4028/www.scientific.net/MSF.416-418.354>
2. Y. Xu, U. Memmert, U. Hartmann, Magnetic field sensors from polycrystalline manganites. *Sens. Actuators A Phys.* **91**(1–2), 26–29 (2001). [https://doi.org/10.1016/S0924-4247\(01\)00493-9](https://doi.org/10.1016/S0924-4247(01)00493-9)
3. L. Li, L. Liang, H. Wu, X. Zhu, One-dimensional perovskite manganite oxide nanostructures: recent developments in synthesis, characterization, transport properties, and applications. *Nanoscale Res. Lett.* **11**(1), 1–17 (2016). <https://doi.org/10.1186/s11671-016-1320-1>
4. F. Ayadi, Y. Regaieg, W. Cheikhrouhou-Koubaa, M. Koubaa, A. Cheikhrouhou, H. Lecoq, S. Nowak, S. Ammar, L. Sicard, Preparation of nanostructured $\text{La}_{0.7}\text{Ca}_{0.3-x}\text{Ba}_x\text{MnO}_3$ ceramics by a combined sol–gel and spark plasma sintering route and resulting magnetocaloric properties. *J. Magn. Magn. Mater.* **381**, 215–219 (2015). <https://doi.org/10.1016/j.jmmm.2014.12.047>
5. N.D. Thorat, K.P. Shinde, S.H. Pawar, K.C. Barick, C.A. Betty, R.S. Ningthoujam, Polyvinyl alcohol: an efficient fuel for synthesis of superparamagnetic LSMO nanoparticles for biomedical application. *Dalton Trans.* **41**(10), 3060–3071 (2012). <https://doi.org/10.1039/c2dt11835a>
6. Y. Tokura, Critical features of colossal magnetoresistive manganites. *Rep. Prog. Phys.* **69**(3), 797 (2006). <https://doi.org/10.1088/0034-4885/69/3/r06>
7. V.K. Pecharsky, K.A. Gschneidner Jr., Tunable magnetic regenerator alloys with a giant magnetocaloric effect for magnetic refrigeration from ~ 20 to ~ 290 K. *Appl. Phys. Lett.* **70**(24), 3299–3301 (1997). <https://doi.org/10.1063/1.119206>
8. L. Morellon, J. Blasco, P.A. Algarabel, M.R. Ibarra, Nature of the first-order antiferromagnetic–ferromagnetic transition in the Gd-rich magnetocaloric compounds $\text{Gd}_5(\text{Si}_x\text{Ge}_{1-x})_4$. *Phys. Rev. B* **62**(2), 1022 (2000). <https://doi.org/10.1103/PhysRevB.62.1022>
9. J.B. Goodenough, Theory of the role of covalence in the perovskite-type manganites $[\text{La}, \text{M}(\text{II})]\text{MnO}_3$. *Phys. Rev.* **100**(2), 564 (1955). <https://doi.org/10.1103/PhysRev.100.564>
10. S. Mori, C.H. Chen, S.W. Cheong, Paired and unpaired charge stripes in the ferromagnetic phase of $\text{La}_{0.5}\text{Ca}_{0.5}\text{MnO}_3$. *Phys. Rev. Lett.* **81**(18), 3972–3975 (1998). <https://doi.org/10.1103/PhysRevLett.81.3972>

11. R.B. Griffiths, Nonanalytic behavior above the critical point in a random Ising ferromagnet. *Phys. Rev. Lett.* **23**(1), 17 (1969). <https://doi.org/10.1103/PhysRevLett.23.17>
12. K. Chu, T. Sun, Y. Liu, G. Dong, S. Zhang, H. Li, X. Pu, X. Yu, X. Liu, Enhanced room temperature coefficient of resistivity (RT-TCR) and broad metal-insulator transition temperature (TMI) of $\text{La}_{0.67}\text{Ca}_{0.33-x}\text{Ag}_x\text{MnO}_3$ polycrystalline ceramics. *Ceram. Int.* **45**(14), 17073–17080 (2019). <https://doi.org/10.1016/j.ceramint.2019.05.259>
13. X. Yu, H. Li, K. Chu, X. Pu, X. Gu, S. Jin, X. Guan, X. Liu, A comparative study on high TCR and MR of $\text{La}_{0.67}\text{Ca}_{0.33}\text{MnO}_3$ polycrystalline ceramics prepared by solid-state and sol-gel methods. *Ceram. Int.* **47**(10), 13469–13479 (2021). <https://doi.org/10.1016/j.ceramint.2021.01.205>
14. A.J. Millis, P.B. Littlewood, B.I. Shraiman, Double exchange alone does not explain the resistivity of $\text{La}_{1-x}\text{Sr}_x\text{MnO}_3$. *Phys. Rev. Lett.* **74**(25), 5144 (1995). <https://doi.org/10.1103/PhysRevLett.74.5144>
15. F. Damay, A. Maignan, C. Martin, B. Raveau, Cation size-temperature phase diagram of the manganites $\text{Ln}_{0.5}\text{Sr}_{0.5}\text{MnO}_3$. *J. Appl. Phys.* **81**(3), 1372–1377 (1997). <https://doi.org/10.1063/1.363873>
16. N. Abdelmoula, E. Dhahri, K. Guidara, J.C. Joubert, Structural magnetic and electrical properties of $\text{La}_{0.6}\text{Ba}_{4-x}\text{Sr}_x\text{MnO}_3$ perovskite. *Phase Transit.* **69**(2), 215–226 (1999). <https://doi.org/10.1080/01411599908208020>
17. M. Bejar, H. Feki, E. Dhahri, M. Ellouze, M. Balli, E.K. Hlil, Effects of substituting divalent by monovalent ion on the physical properties of $\text{La}_{0.7}\text{Ca}_{0.3-x}\text{K}_x\text{MnO}_3$ compounds. *J. Magn. Magn. Mater.* **316**(2), e707–e709 (2007). <https://doi.org/10.1016/j.jmmm.2007.03.067>
18. A.K.M.A. Hossain, L.F. Cohen, T. Kodenkandeth, J. MacManus-Driscoll, N.M. Alford, Influence of oxygen vacancies on magnetoresistance properties of bulk $\text{La}_{0.67}\text{Ca}_{0.33}\text{MnO}_{3-\delta}$. *J. Magn. Magn. Mater.* **195**(1), 31–36 (1999). [https://doi.org/10.1016/S0304-8853\(98\)00749-5](https://doi.org/10.1016/S0304-8853(98)00749-5)
19. N. Sdiri, M. Bejar, M. Hussein, S. Mazen, E. Dhahri, Effect of the oxygen deficiency in physical properties of $\text{La}_{0.7}\text{Ca}_{0.25}\text{Sr}_{0.05}\text{MnO}_{3-\delta}$ oxides ($0 \leq \delta \leq 0.15$). *J. Magn. Magn. Mater.* **316**(2), e703–e706 (2007). <https://doi.org/10.1016/j.jmmm.2007.03.066>
20. H. Song, W. Kim, S.-J. Kwon, J. Kang, Magnetic and electronic properties of transition-metal-substituted perovskite manganites— $\text{La}_{0.7}\text{Ca}_{0.3}\text{Mn}_{0.95}\text{X}_{0.05}\text{O}_3$ (X = Fe, Co, Ni). *J. Appl. Phys.* **89**(6), 3398–3402 (2001). <https://doi.org/10.1063/1.1350417>
21. Y. Sun, T. Wei, X. Xiaojun, Z. Yuheng, Extraordinary colossal magnetoresistance in $\text{La}_{0.67}\text{Ca}_{0.33}\text{Mn}_{1-x}\text{Cr}_x\text{O}_3$ ($x \leq 0.3$). *J. Magn. Magn. Mater.* (2001). [https://doi.org/10.1016/S0304-8853\(01\)00155-x](https://doi.org/10.1016/S0304-8853(01)00155-x)
22. R.-W. Li, J.-R. Sun, Z.-H. Wang, S.-Y. Zhang, B.-G. Shen, Magnetic and transport properties of Sn-doped $\text{La}_{0.5}\text{Ca}_{0.5}\text{MnO}_3$. *J. Phys. D.* **33**(16), 1982 (2000). <https://doi.org/10.1088/0022-3727/33/16/308>
23. T.M. Tank, V. Sridharan, S.S. Samatham, V. Ganesan, S.P. Sanyal, Effect of Sn substitution on structural and transport properties of $(\text{La}_{0.67}\text{Sr}_{0.33})\text{MnO}_3$. *AIP Conf. Proc.* **1536**(1), 573–574 (2013). <https://doi.org/10.1063/v1536.frontmatter>
24. N. Kallel, K. Fröhlich, S. Pignard, M. Oumezzine, H. Vincent, Structure, magnetic and magnetoresistive properties of $\text{La}_{0.7}\text{Sr}_{0.3}\text{Mn}_{1-x}\text{Sn}_x\text{O}_3$ samples ($0 \leq x \leq 0.20$). *J. Alloys Compd.* **399**(1–2), 20–26 (2005). <https://doi.org/10.1016/j.jallcom.2005.03.019>
25. S.R. Lee, M.S. Anwar, F. Ahmed, B.H. Koo, Effect of sintering temperature on structure, magnetic and magnetocaloric properties of $\text{La}_{0.6}\text{Ca}_{0.4}\text{MnO}_3$ manganite. *Trans. Nonferrous Met. Soc. China* **24**, s141–s145 (2014). [https://doi.org/10.1016/S1003-6326\(14\)63301-x](https://doi.org/10.1016/S1003-6326(14)63301-x)
26. G. Venkataiah, D.C. Krishna, M. Vithal, S.S. Rao, S.V. Bhat, V. Prasad, S.V. Subramanyam, P.V. Reddy, Effect of sintering temperature on electrical transport properties of $\text{La}_{0.67}\text{Ca}_{0.33}\text{MnO}_3$. *Phys. B Condens. Matter* **357**(3–4), 370–379 (2005). <https://doi.org/10.1016/j.physb.2004.12.001>
27. S.V. Trukhanov, D.P. Kozlenko, A.V. Trukhanov, High hydrostatic pressure effect on magnetic state of anion-deficient $\text{La}_{0.70}\text{Sr}_{0.30}\text{MnO}_x$ perovskite manganites. *J. Magn. Magn. Mater.* **320**(14), e88–e91 (2008). <https://doi.org/10.1016/j.jmmm.2008.02.021>
28. W. Chérif, M. Ellouze, F. Elhalouani, A.-F. Lehlooh, Synthesis and characterization of fine particles of $\text{La}_{0.7}\text{Ca}_{0.3}\text{MnO}_3$ prepared by the mechanical ball milling method. *Eur. Phys. J. Plus* **127**(7), 1–7 (2012). <https://doi.org/10.1140/epjp/i2012-12073-3>
29. N. Kumar, A. Shukla, N. Kumar, R.N.P. Choudhary, Effects of milling time on structural, electrical and ferroelectric features of mechanothermally synthesized multi-doped bismuth ferrite. *Appl. Phys. A* **126**(3), 1–15 (2020). <https://doi.org/10.1007/s00339-020-3365-3>
30. W. Boujelben, M. Ellouze, A. Cheikh-Rouhou, J. Pierre, J.C. Joubert, Effect of quenching on magnetoresistance properties in the $\text{Pr}_{0.5}\text{Sr}_{0.5}\text{MnO}_3$ perovskite manganite. *J. Solid State Chem.* **165**(2), 375–380 (2002). <https://doi.org/10.1006/jssc.2002.9555>
31. A. Krichene, W. Boujelben, A. Cheikhrouhou, Quenching effects on correlation between electrical and magnetic properties in $\text{Pr}_{0.5}\text{Sr}_{0.5}\text{MnO}_3$ polycrystalline manganites. *Phys. B* **433**, 122–126 (2014). <https://doi.org/10.1016/j.physb.2013.10.026>
32. H.M. Rietveld, A profile refinement method for nuclear and magnetic structures. *J. Appl. Crystallogr.* **2**(2), 65–71 (1969). <https://doi.org/10.1107/S0021889869006558>
33. M. Khlifi, M. Bejar, O.E.L. Sadek, E. Dhahri, M.A. Ahmed, E.K. Hlil, Structural, magnetic and magnetocaloric properties of the lanthanum deficient in $\text{La}_{0.8}\text{Ca}_{0.2-x}\text{MnO}_3$ ($x = 0-0.20$) manganites oxides. *J. Alloys Compd.* **509**(27), 7410–7415 (2011). <https://doi.org/10.1016/j.jallcom.2011.04.049>
34. K. Momma, F. Izumi, VESTA 3 for three-dimensional visualization of crystal, volumetric and morphology data. *J. Appl. Crystallogr.* **44**(6), 1272–1276 (2011). <https://doi.org/10.1107/S0021889811038970>
35. J.M.D. Coey, M. Viret, S. Von Molnar, Mixed-valence manganites. *Adv. Phys.* **48**(2), 167–293 (1999). <https://doi.org/10.1080/000187399243455>
36. R.D. Shannon, Revised effective ionic radii and systematic studies of interatomic distances in halides and chalcogenides. *Acta Crystallogr. Sect. A* **32**(5), 751–767 (1976). <https://doi.org/10.1107/S0567739476001551>
37. Y. Tokura, Y. Tomioka, Colossal magnetoresistive manganites. *J. Magn. Magn. Mater.* **200**(1–3), 1–23 (1999). [https://doi.org/10.1016/S0304-8853\(99\)00352-2](https://doi.org/10.1016/S0304-8853(99)00352-2)
38. D. Kumar, N.K. Verma, C.B. Singh, A.K. Singh, Evolution of structural characteristics of $\text{Nd}_{0.7}\text{Ba}_{0.3}\text{MnO}_3$ perovskite manganite as a function of crystallite size. *AIP Conf. Proc.* **2009**(1), 20013 (2018). <https://doi.org/10.1063/1.5052082>
39. S. Bouzidi, M.A. Gdaiem, S. Rebaoui, J. Dhahri, E.K. Hlil, Large magnetocaloric effect in $\text{La}_{0.75}\text{Ca}_{0.25-x}\text{Na}_x\text{MnO}_3$ ($0 \leq x \leq 0.10$) manganites. *Appl. Phys. A* **126**(1), 1–16 (2020). <https://doi.org/10.1007/s00339-019-3219-z>
40. M. Mazaheri, M. Akhavan, Preparation and characterization of nano-polycrystalline lanthanum-based manganite ($\text{La}_{1-y}\text{K}_y$) $_{0.7}\text{Ca}_{0.3}\text{MnO}_3$. *Phys. B Condens. Matter* **405**(1), 72–76 (2010). <https://doi.org/10.1016/j.physb.2009.08.033>
41. U. Holzwarth, N. Gibson, The Scherrer equation versus the 'Debye-Scherrer equation'. *Nat. Nanotechnol.* **6**(9), 534 (2011). <https://doi.org/10.1038/nnano.2011.145>

42. G.K. Williamson, W.H. Hall, X-ray line broadening from filed aluminium and wolfram. *Acta Metall.* **1**(1), 22–31 (1953). [https://doi.org/10.1016/0001-6160\(53\)90006-6](https://doi.org/10.1016/0001-6160(53)90006-6)
43. I.A.U. Shah, I. Mohd, Structural stability improvement, Williamson Hall analysis and band-gap tailoring through A-site Sr doping in rare earth based double perovskite $\text{La}_2\text{NiMnO}_6$. *Rare Met.* **38**(9), 805–813 (2019). <https://doi.org/10.1007/s12598-019-01207-4>
44. A. Dhahri, M. Jemmali, E. Dhahri, M.A. Valente, Structural characterization, magnetic, magnetocaloric properties and phenomenological model in manganite $\text{La}_{0.75}\text{Sr}_{0.1}\text{Ca}_{0.15}\text{MnO}_3$ compound. *J. Alloys Compd.* **638**, 221–227 (2015). <https://doi.org/10.1016/j.jallcom.2015.01.314>
45. C.T. Rueden, J. Schindelin, M.C. Hiner, B.E. DeZonia, A.E. Walter, E.T. Arena, K.W. Eliceiri, ImageJ2: ImageJ for the next generation of scientific image data. *BMC Bioinform.* **18**(1), 1–26 (2017). <https://doi.org/10.1186/s12859-017-1934-z>
46. J. Ye, C. Bu, Z. Han, G. He, J. Li, Y. Chen, Microstructural evolution and infrared radiation property of $\text{Ca}^{2+}\text{-Cr}^{3+}$ doped LaAlO_3 in the presence of SiO_2 . *Mater. Lett.* **171**, 55–58 (2016). <https://doi.org/10.1016/j.matlet.2016.02.031>
47. N. Choudhary, M.K. Verma, N.D. Sharma, S. Sharma, D. Singh, Correlation between magnetic and transport properties of rare earth doped perovskite manganites $\text{La}_{0.6}\text{R}_{0.1}\text{Ca}_{0.3}\text{MnO}_3$ (R = La, Nd, Sm, Gd, and Dy) synthesized by Pechini process. *Mater. Chem. Phys.* **242**, 122482 (2020). <https://doi.org/10.1016/j.matchemphys.2019.122482>
48. R. Rao, Y.Y. Han, X.C. Kan, X. Zhang, M. Wang, N.X. Qian, G.H. Zheng, Y.Q. Ma, Magnetic property under the pressure and electrical transport behavior under the magnetic field for the perovskite manganite $\text{La}_{0.7}\text{Ca}_{0.3}\text{MnO}_3$. *J. Alloys Compd.* **837**, 155476 (2020). <https://doi.org/10.1016/j.jallcom.2020.155476>
49. Y. Regaieg, M. Kouba, W.C. Kouba, A. Cheikhrouhou, L. Sicard, S. Ammar-Merah, F. Herbst, Structure and magnetocaloric properties of $\text{La}_{0.8}\text{Ag}_{0.2-x}\text{K}_x\text{MnO}_3$ perovskite manganites. *Mater. Chem. Phys.* **132**(2–3), 839–845 (2012). <https://doi.org/10.1016/j.matchemphys.2011.12.021>
50. I. Chihri, M. Baazaoui, S. Mahjoub, W. Cheikhrouhou-Koubaa, M. Oumezzine, K. Farah, Study of the magnetic and magnetocaloric properties of new perovskite-type materials: $\text{La}_{0.6}\text{Ba}_{0.2}\text{Sr}_{0.2}\text{Mn}_{1-x}\text{Fe}_x\text{O}_3$. *Appl. Phys. A* **125**(9), 1–7 (2019). <https://doi.org/10.1007/s00339-019-2909-x>
51. R. Felhi, M. Koubaa, W. Cheikhrouhou-Koubaa, A. Cheikhrouhou, Structural, magnetic, magnetocaloric and critical behavior investigations of $\text{La}_{0.65}\text{Dy}_{0.05}\text{Sr}_{0.3}\text{MnO}_3$ manganite. *J. Alloys Compd.* **726**, 1236–1245 (2017). <https://doi.org/10.1016/j.jallcom.2017.08.080>
52. A. Dhahri, M. Jemmali, K. Taibi, E. Dhahri, E.K. Hlil, Structural, magnetic and magnetocaloric properties of $\text{La}_{0.7}\text{Ca}_{0.2}\text{Sr}_{0.1}\text{Mn}_{1-x}\text{Cr}_x\text{O}_3$ compounds with $x = 0, 0.05$ and 0.1 . *J. Alloys Compd.* **618**, 488–496 (2015). <https://doi.org/10.1016/j.jallcom.2014.08.117>
53. A. Tozri, E. Dhahri, Structural and magnetotransport properties of (La, Pr)-Ba manganites. *J. Alloys Compd.* **783**, 718–728 (2019). <https://doi.org/10.1016/j.jallcom.2018.12.303>
54. K. Dhahri, N. Dhahri, J. Dhahri, K. Taibi, E.K. Hlil, Effect of (Al, Sn) doping on structural, magnetic and magnetocaloric properties of $\text{La}_{0.7}\text{Ca}_{0.1}\text{Pb}_{0.2}\text{Mn}_{1-x-y}\text{Al}_x\text{Sn}_y\text{O}_3$ ($0 \leq x, y \leq 0.075$) manganites. *J. Alloys Compd.* **699**, 619–626 (2017). <https://doi.org/10.1016/j.jallcom.2016.12.324>
55. M. Dhahri, A. Zaidi, K. Cherif, J. Dhahri, E.K. Hlil, Effect of indium substitution on structural, magnetic and magnetocaloric properties of $\text{La}_{0.5}\text{Sm}_{0.1}\text{Sr}_{0.4}\text{Mn}_{1-x}\text{In}_x\text{O}_3$ ($0 \leq x \leq 0.1$) manganites. *J. Alloys Compd.* **691**, 578–586 (2017). <https://doi.org/10.1016/j.jallcom.2016.08.268>
56. C. Kittel, *Introduction to Solid State Physics*, 6th edn. (Uno, N. Tsuya, A. Morita J. Yamashita, Maruzen, 1986), pp.124–129
57. R.C. Sahoo, S. Das, S.K. Giri, D. Paladhi, T.K. Nath, Size modulated Griffiths phase and spin dynamics in double perovskite $\text{Sm}_{1.5}\text{Ca}_{0.5}\text{CoMnO}_6$. *J. Magn. Magn. Mater.* **469**, 161–170 (2019). <https://doi.org/10.1016/j.jmmm.2018.08.060>
58. M. Bourguiba, M.A. Gdaiem, M. Chafra, E.K. Hlil, H. Belmabrouk, A. Bajahzar, Effect of titanium substitution on the structural, magnetic and magnetocaloric properties of $\text{La}_{0.67}\text{Ba}_{0.25}\text{Ca}_{0.08}\text{MnO}_3$ perovskite manganites. *Appl. Phys. A* **125**(6), 1–16 (2019). <https://doi.org/10.1007/s00339-019-2665-y>
59. P. Kameli, H. Salamati, A. Aezami, Influence of grain size on magnetic and transport properties of polycrystalline $\text{La}_{0.8}\text{Sr}_{0.2}\text{MnO}_3$ manganites. *J. Alloys Compd.* **450**(1–2), 7–11 (2008). <https://doi.org/10.1016/j.jallcom.2006.10.078>
60. V. Dyakonov, A. Slawka-Waniewska, N. Nedelko, E. Zubov, V. Mikhaylov, K. Piotrowski, A. Szytuta, S. Baran, W. Bazela, Z. Kravchenko, P. Aleshkevich, A. Pashchenko, K. Dyakonov, V. Varyukhin, H. Szymczak, Magnetic, resonance and transport properties of nanopowder of $\text{La}_{0.7}\text{Sr}_{0.3}\text{MnO}_3$ manganites. *J. Magn. Magn. Mater.* **322**(20), 3072–3079 (2010). <https://doi.org/10.1016/j.jmmm.2010.05.032>
61. C. Zener, Interaction between the d-shells in the transition metals. II. Ferromagnetic compounds of manganese with perovskite structure. *Phys. Rev.* **82**(3), 403 (1951). <https://doi.org/10.1103/PhysRev.82.403>
62. P.-G. De Gennes, Effects of double exchange in magnetic crystals. *Phys. Rev.* **118**(1), 141 (1960). <https://doi.org/10.1103/PhysRev.118.141>
63. R. Thaljaoui, D. Szewczyk, Electrical and thermal properties of $\text{Pr}_{0.6}\text{Sr}_{0.4-x}\text{Ag}_x\text{MnO}_3$ ($x = 0.05$ and 0.1) manganite. *J. Mater. Sci.* **55**(16), 6761–6770 (2020). <https://doi.org/10.1007/s10853-020-04484-y>
64. P.G. Radaelli, G. Iannone, M. Marezio, H.Y. Hwang, S.W. Cheong, J.D. Jorgensen, D.N. Argyriou, Structural effects on the magnetic and transport properties of perovskite $\text{A}_{1-x}\text{A}'_x\text{MnO}_3$ ($x = 0.25, 0.30$). *Phys. Rev. B* **56**(13), 8265 (1997). <https://doi.org/10.1103/PhysRevB.56.8265>
65. C. Cui, T.A. Tyson, Correlations between pressure and bandwidth effects in metal–insulator transitions in manganites. *Appl. Phys. Lett.* **84**(6), 942–944 (2004). <https://doi.org/10.1063/1.1646212>
66. W. A. Harrison. *Electronic Structure and the Properties of Solids*/ Ed. by WH Freeman and Company. San Fr. (1980)
67. A. A. Gómez Zapata. Determination of the relationship between magnetocaloric effect and electrical properties in polycrystalline samples of $\text{La}_{0.7}\text{Ca}_{0.3}\text{Mn}_{1-x}\text{Ni}_x\text{O}_3$ ($x = 0, 0.02, 0.07, 0.1$). PhD Dissertation, National University of Colombia. (2019)
68. A. Goyal, M. Rajeswari, R. Shreekala, S.E. Lofland, S.M. Bhaqat, T. Boettcher, C. Kwon, R. Ramesh, T. Venkatesana, Material characteristics of perovskite manganese oxide thin films for bolometric applications. *Appl. Phys. Lett.* **71**(17), 2535–2537 (1997). <https://doi.org/10.1063/1.120427>
69. S. Vadnala, T.D. Rao, P. Pal, S. Asthana, Study of structural effect on Eu-substituted LSMO manganite for high temperature coefficient of resistance. *Phys. B Condens. Matter* **448**, 277–280 (2014). <https://doi.org/10.1016/j.physb.2014.04.029>
70. R.J. Choudhary, A.S. Ogale, S.R. Shinde, S. Hullavard, S.B. Ogale, T. Venkatesan, R.N. Bathe, S.I. Patil, R. Kumar, Evaluation of manganite films on silicon for uncooled bolometric applications. *Appl. Phys. Lett.* **84**(19), 3846–3848 (2004). <https://doi.org/10.1063/1.1748837>
71. A. Pal, B.S. Nagaraja, K.J. Rachana, K.V. Supriya, D. Kekuda, A. Rao, C.R. Li, Y.K. Kuo, Enhancement of temperature coefficient of resistance (TCR) and magnetoresistance (MR) of $\text{La}_{0.67-x}\text{RE}_x\text{Ca}_{0.33}\text{MnO}_3$ ($x = 0, 0.1$; RE = Gd, Nd, Sm) system via

- rare-earth substitution. *Mater. Res. Express* **7**(3), 36102 (2020). <https://doi.org/10.1088/2053-1591/ab7c20>
72. S. Boufligha, N. Mahamdioua, F. Denbri, F. Meriche, S.P. Altintas, C. Terzioğlu, Synthesis and experimental study of structure, magnetotransport properties and temperature coefficient of resistance of $\text{La}_{0.7}\text{Ca}_{0.18}\text{Ba}_{0.12}\text{Mn}_{0.95}\text{Sn}_{0.05}\text{O}_3$. *J. Low Temp. Phys.* (2021). <https://doi.org/10.1007/s10909-021-02645-0>
 73. Y. Sun, X. Xu, Y. Zhang, Variable-range hopping of small polarons in mixed-valence manganites. *J. Phys. Condens. Matter* **12**(50), 10475 (2000). <https://doi.org/10.1088/0953-8984/12/50/309>
 74. M. Oumezzine, O. Peña, T. Guizouarn, R. Lebullenger, M. Oumezzine, Impact of the sintering temperature on the structural, magnetic and electrical transport properties of doped $\text{La}_{0.67}\text{Ba}_{0.33}\text{Mn}_{0.9}\text{Cr}_{0.1}\text{O}_3$ manganite. *J. Magn. Magn. Mater.* **324**(18), 2821–2828 (2012). <https://doi.org/10.1016/j.jmmm.2012.04.017>
 75. G. Venkataiah, P.V. Reddy, Structural, magnetic and magnetotransport behavior of some Nd-based perovskite manganites. *Solid State Commun.* **136**(2), 114–119 (2005). <https://doi.org/10.1016/j.ssc.2005.04.014>
 76. M. Ziese, Searching for quantum interference effects in $\text{La}_{0.7}\text{Ca}_{0.3}\text{MnO}_3$ films on SrTiO_3 . *Phys. Rev. B* **68**(13), 132411 (2003). <https://doi.org/10.1103/PhysRevB.68.132411>
 77. P. Schiffer, A.P. Ramirez, W. Bao, S.-W. Cheong, Low temperature magnetoresistance and the magnetic phase diagram of $\text{La}_{1-x}\text{Ca}_x\text{MnO}_3$. *Phys. Rev. Lett.* **75**(18), 3336 (1995). <https://doi.org/10.1103/PhysRevLett.75.3336>
 78. Y.K. Lakshmi, P.V. Reddy, Electrical behavior of some silver-doped lanthanum-based CMR materials. *J. Magn. Magn. Mater.* **321**(9), 1240–1245 (2009). <https://doi.org/10.1016/j.jmmm.2008.11.012>
 79. A. Banerjee, S. Pal, S. Bhattacharya, B.K. Chaudhuri, H.D. Yang, Particle size and magnetic field dependent resistivity and thermoelectric power of $\text{La}_{0.5}\text{Pb}_{0.5}\text{MnO}_3$ above and below metal–insulator transition. *J. Appl. Phys.* **91**(8), 5125–5134 (2002). <https://doi.org/10.1063/1.1459618>
 80. R.L. Zhang, W.H. Song, Y.Q. Ma, J. Yang, B.C. Zhao, Z.G. Sheng, J.M. Dai, Y.P. Sun, Influence of Co doping on the charge-ordering state of the bilayered manganite $\text{LaSr}_2\text{Mn}_2\text{O}_7$. *Phys. Rev. B* **70**(22), 224418 (2004). <https://doi.org/10.1103/PhysRevB.70.224418>
 81. G. Huo, Q. Yang, F. Dong, D. Song, Structural, magnetic and electrical transport properties for a series of $\text{La}_{1-x}\text{Sr}_x\text{Fe}_{1-x}\text{Mn}_x\text{O}_3$ ($0.3 \leq x \leq 0.7$) compounds. *J. Alloys Compd.* **464**(1–2), 42–46 (2008). <https://doi.org/10.1016/j.jallcom.2007.10.031>
 82. N. Mahamdioua, A. Amira, Y. Boudjadja, A. Saouadel, S.P. Altintas, A. Varilci, C. Terzioğlu, Magneto-conductive mechanisms in the La-site doped double-layered $\text{La}_{1.4}\text{Ca}_{1.6}\text{Mn}_2\text{O}_7$ manganites. *Phys. B Condens. Matter* **500**, 77–84 (2016). <https://doi.org/10.1016/j.physb.2016.07.011>
 83. D. Joung, S.I. Khondaker, Efros-Shklovskii variable-range hopping in reduced graphene oxide sheets of varying carbon s p 2 fraction. *Phys. Rev. B* **86**(23), 235423 (2012). <https://doi.org/10.1103/PhysRevB.86.235423>
 84. S. Hcini, S. Khadhraoui, S. Zemni, A. Triki, H. Rahmouni, M. Boudard, M. Oumezzine, Percolation model of the temperature dependence of resistivity in $\text{Pr}_{0.67}\text{A}_{0.33}\text{MnO}_3$ (A= Ba or Sr) manganites. *J. Supercond. Nov. Magn.* **26**(6), 2181–2185 (2013). <https://doi.org/10.1007/s10948-012-1812-x>
 85. Z. Zainuddin, A.H. Shaari, Structural and electrical transport properties of $\text{La}_{0.67}\text{Ba}_{0.33}\text{Mn}_{1-y}\text{Ti}_y\text{O}_3$ ceramics. *Adv. Mater. Res.* **501**, 86–90 (2012). <https://doi.org/10.4028/www.scientific.net/amr.501.86>
 86. A. Modi, M.A. Bhat, D.K. Pandey, S. Bhattacharya, N.K. Gaur, G.S. Okram, Structural, magnetotransport and thermal properties of Sm substituted $\text{La}_{0.7-x}\text{Sm}_x\text{Ba}_{0.3}\text{MnO}_3$ ($0 \leq x \leq 0.2$) manganites. *J. Magn. Magn. Mater.* **424**, 459–466 (2017). <https://doi.org/10.1016/j.jmmm.2016.10.048>
 87. M. Viret, L. Ranno, J.M.D. Coey, Magnetic localization in mixed-valence manganites. *Phys. Rev. B* **55**(13), 8067 (1997). <https://doi.org/10.1103/PhysRevB.55.8067>
 88. V. Ravindranath, M.R. Rao, G. Rangarajan, Y. Lu, J. Klein, R. Klingeler, S. Uhlenbruck, B. Buchner, R. Gross, Magnetotransport studies and mechanism of Ho- and Y-doped $\text{La}_{0.7}\text{Ca}_{0.3}\text{MnO}_3$. *Phys. Rev. B* **63**(18), 184434 (2001). <https://doi.org/10.1103/PhysRevB.63.184434>
 89. M. Ziese, C. Srinithirawong, Polaronic effects on the resistivity of manganite thin films. *Phys. Rev. B* **58**(17), 11519 (1998). <https://doi.org/10.1103/PhysRevB.58.11519>
 90. A. Modi, M.A. Bhat, S. Bhattacharya, N.K. Gaur, Investigation of structural and some physical properties of Cr substituted polycrystalline $\text{Eu}_{0.5}\text{Sr}_{0.5}\text{Mn}_{1-x}\text{Cr}_x\text{O}_3$ ($0 \leq x \leq 0.1$) manganites. *J. Mater. Sci. Mater. Electron.* **27**(9), 8899–8905 (2016). <https://doi.org/10.1007/s10854-016-4916-4>
 91. C.L. Zhang, X.J. Chen, C.C. Almasan, J.S. Gardner, J.L. Sarrao, Low-temperature electrical transport in bilayer manganite $\text{La}_{1.2}\text{Sr}_{1.8}\text{Mn}_2\text{O}_7$. *Phys. Rev. B* **65**(13), 134439 (2002). <https://doi.org/10.1103/PhysRevB.65.134439>
 92. X.J. Chen, C.L. Zhang, J.S. Gardner, J.L. Sarrao, C.C. Almasan, Variable-range-hopping conductivity of the half-doped bilayer manganite $\text{LaSr}_2\text{Mn}_2\text{O}_7$. *Phys. Rev. B* **68**(6), 64405 (2003). <https://doi.org/10.1103/PhysRevB.68.064405>
 93. J.C. Debnath, J. Wang, Magnetic and electrical response of Co-doped $\text{La}_{0.7}\text{Ca}_{0.3}\text{MnO}_3$ manganites/insulator system. *Phys. B* **504**, 58–62 (2017). <https://doi.org/10.1016/j.physb.2016.10.017>
 94. A.M. Ahmed, G. Papavassiliou, H.F. Mohamed, E.M.M. Ibrahim, Structural, magnetic and electronic properties on the Li-doped manganites. *J. Magn. Magn. Mater.* **392**, 27–41 (2015). <https://doi.org/10.1016/j.jmmm.2015.05.004>

Publisher's Note Springer Nature remains neutral with regard to jurisdictional claims in published maps and institutional affiliations.

Springer Nature or its licensor (e.g. a society or other partner) holds exclusive rights to this article under a publishing agreement with the author(s) or other rightsholder(s); author self-archiving of the accepted manuscript version of this article is solely governed by the terms of such publishing agreement and applicable law.